Wave field properties in tropical cyclones from the spectral observation of the CFOSAT/SWIM spaceborne instrument

Eva Le Merle, Danièle Hauser, C. Yang

Wave field properties in tropical cyclones from the spectral observation of the CFOSAT/SWIM spaceborne instrument

E. Le Merle[1], D. Hauser[2], C.Yang[1]

[1]Institute of Marine Sciences, National Research Council
[2]LATMOS (CNRS, Université Versailles Saint-Quentin, Paris Sorbonne Université)

Key Points:

- Ocean wave spectra measured with the CFOSAT/SWIM spaceborne instrument are investigated under tropical cyclones over a three-year period.
- The asymmetry of the wave parameters depends on the ratio of the maximum sustained wind speed and the TCs speed.
- The shape of the omni- and directional spectra varies according to the TC class and to the distance from the center of the TC.

Corresponding author: Eva Le Merle, eva.lemerle@artov.ismar.cnr.it

Abstract

Tropical cyclones (TCs) are extreme events that generate, because of their movement, complex wave fields. The SWIM instrument is a real aperture radar that provides unprecedented detailed information about the waves with dominant wavelength between 70 and 500 m in all directions at the global scale. In this study we collocated 3 years of SWIM data with 67 TCs in the Northern Hemisphere to analyze the impact of the TC characteristics on the wave field. TCs have been classified into three different classes (slow, moderate speed and fast) estimated based on the ratio between the maximum sustained wind and the displacement velocity. In order to analyze the characteristics of the wave field in the space domain, the observations have been separated according to the distance with the TC center and the quadrant. The results show that the characteristics of the TCs impact the wave field: the more favorable conditions for trapped wave phenomenon appears to be under moderate speed TC conditions. In slow and moderate speed TCs, close to the center the directional spectra are mono-modal and tend to become bi- or multi-modal when the distance to the center increases whereas in fast-moving TCs, the directional spectra are always bi- or multi-modal. Omni-directional spectra show similarities with fetch-limited spectra in slow and moderate speed TCs whereas in fast-moving TCs, because of the presence of mixed-sea, the decrease of energy with frequency is less steep than in fetch-limited conditions.

Plain Language Summary

Tropical cyclones (TCs) are extreme meteorological events, causing in-land damages such as inundations, but also storm surges due to the intense sea states. Even if forecast models provide satisfying estimation of the sea state under TC conditions, we still need observations to improve their representation and evolution during these events. The France Oceanography Satellite (CFOSAT), carries a real aperture radar that provides detailed wave energy distribution with direction and wavelength at the global scale. In this study we choose to use this information to study the impact of the TC characteristics on the wave field. To do so, we classified TCs into three classes according to their displacement velocity (slow, moderate speed and fast). CFOSAT observations confirm some of the conclusions obtained in previous studies such as the asymmetry of the wave height previously observed with airborne and buoy measurements. Moreover, in slow-moving and moderate speed TCs, close to the TC center, the wave field show some similarities with wave field obtained in conditions of wave growth by stable wind. However, in fast-moving TCs the wave field is more variable with the presence of several wave systems interacting between each other.

1 Introduction

Tropical cyclones (TCs) are extreme meteorological events which generate extreme winds, waves and precipitations. The very high waves generated by the cyclones impact the maritime navigation, the risk in coastal areas and modify the ocean-atmosphere interactions (Prakash et al., 2019; Zhang et al., 2021; Lin et al., 2021; Fan et al., 2020). Therefore, a detailed description and a better understanding of the wave field properties under TC conditions is a topic of great relevance to oceanographic research and engineering applications.

Tropical cyclones are moving systems characterized by rotational winds with complex features such as radial gradients and asymmetry, with usually stronger winds on the right (left) side of the TC displacement direction in the Northern (Southern) Hemisphere. These complex wind fields generate wave fields with even more complex structures. The wave field characteristic most often cited in the literature is the significant wave height (Hs) asymmetry characterized by the presence of the highest waves on the right side of the TCs (Young, 2006; Kudryavtsev et al., 2015; Shi et al., 2021). This feature is explained

by the concept of "extended fetch" for waves which travel in the same direction as the cyclone (Young, 1998) or by the "trapped waves" concept related to a resonance phenomenon (Bowyer & MacAfee, 2005) that occurs when the wind-generated waves cannot escape from the cyclone area because their group velocity remains of the order of the displacement velocity of the system. Moon et al. (2003), who analyze the wave field of TC Bonnie at two different stages, suggest that the hurricane-generated wave field is influenced not only by the radius of maximum wind but also by the TC displacement velocity.This conclusion was also proposed by Young (1998, 2017), although Shi et al. (2021) found that the asymmetric behavior of the significant wave height mainly depends on the TC intensity. In order to better characterize the wave field behavior under TC conditions, Kudryavtsev et al. (2015) proposed a simplified model, parameterized in terms of maximum wind and displacement speed, which explains this significant wave height asymmetry even in absence of wind field asymmetry. Hell et al. (2021) and Kudryavtsev et al. (2021a) proposed numerical model of wave parameter evolution in a Lagrangian frame within moving TCs. Despite numerical efforts to further document and represent the wave field behavior and to further validate these theoretical concepts, additional spectral wave observations are required and need to be analyzed under different classes of TCs. This paper fits into this context.

In addition to the significant wave height, other wave parameters and the distribution of the wave energy also need to be investigated. In the early 2000s, thanks to observations from the airborne Scanning Radar Altimeter (SAR), Wright et al. (2001) showed that additionally to the Hs field, the frequency and the direction field of the dominant waves was also asymmetric. Moreover, they analyzed the energy distribution of the wave spectra and concluded that in the right front quadrant the wave field tended to be unidirectional, more or less aligned with the wind direction, whereas in the other quadrants, bi- or tri-modal wave systems with similar wavelength were observed. This was later confirmed by Hu and Chen (2011) who analyzed directional buoy data during the passage of 7 TCs, and Hwang and Walsh (2018) who extended this analysis of SRA spectral observations within 11 cyclones. Esquivel-Trava et al. (2015) also provided additional details on the wave energy distribution by classifying directional spectra from buoy data within 14 TCs according to their distance from the TC center.

Several studies such as Esquivel-Trava et al. (2015) and Tamizi and Young (2020) have shown that, despite the presence of mixed-sea situations and an important dispersion, the shape of the omni-directional frequency spectra and the self-similar non-dimensional law relating wave energy to the wave frequency were close to those in conditions of wind-wave growing under fetch-limited conditions. For example, under TC conditions, the omni-directional spectra are characterized by a mono-modal spectrum shape in frequency and a constant spectral slope on the right of the peak, even if the spectra are sharper than those under fetch-limited conditions. The results of Hwang et al. (2017) indicate that this spectral slope may vary according to the sectors of the TCs. Young (2006) (among others) justified this mono-modal spectrum shape in frequency despite the presence of several energetic wave components separated in directions by the non-linear interactions between the waves. The modeling work of Hu and Chen (2011) indicates however that even if the non-linear interactions are important in particular in the right quadrant, the other mechanisms, such as wind input and dissipation, cannot be neglected. In addition, although the parametric model proposed by Kudryavtsev et al. (2021a) which estimates wave spectra parameters in a Lagrangian approach does not take into account explicitly the non-linear interactions, the consistency of their results with observation is rather convincing. On the other hand, the numerical simulations of Tamizi et al. (2021)show that at distances close to the center of the TC, except in the right front quadrant, the non-linear interactions are crucial to explain the mono-modal shape of the spectrum.

In order to further characterize, understand and model the wave field associated with tropical cyclone, there is a need to continue the analysis of wave spectral proper-

ties within tropical cyclones. Advances in space instrumentation provide systematic observations of the wave field on large spatial and temporal scales. In particular, the Surface Wave Investigation and Monitoring (SWIM) instrument on-board the China-France Oceanography Satellite (CFOSAT) mission, launched in space in October 2018, now provides globally, and on a systematic basis, directional ocean wave spectra every 90 km with detailed wave information with dominant wavelength between 70 and 500 m (Hauser et al., 2021). Some studies already showed that the SWIM observations are useful in several ways, such as improving wave forecasting models (Aouf et al., 2021), analyzing the directional properties of the wave or the probability of extreme waves at the global scale (Le Merle et al., 2021) or estimating the wave induced stress at the global scale (Chen et al., 2020). Oruba et al. (2022) also shows that, as SWIM observations are not affected by the cutoff effect as the SAR observations, SWIM provides complementary information in comparison to SAR instruments to document wave spectra in moderate and high sea state conditions.

In this paper, by using the SWIM observations, we further investigate the distribution of ocean wave spectra and of their main parameters, obtained under TC conditions. The analyzed data set spans over more than three years of observations between May 2019 and September 2022 during which 67 TCs with maximum sustained wind speed stronger than 30 m/s occurring in the Northern Hemisphere are observed. The originality of our study is to analyze the ocean wave spectra properties according to the TC characteristics such as the relative displacement velocity. This was chosen to better characterize the impact of the displacement velocity and the maximum wind speed on the wave parameter asymmetry. We defined three different classes of TCs according to the ratio of the maximum sustained wind speed to the displacement velocity of the TC: slow, moderate speed and fast-moving TCs (see section 2.3). For each class, the spectral shape of the directional and omni-directional ocean wave spectra is investigated as well as the wave parameters.

The paper is organized as follows. In section 2, the data sets and the methods are introduced. Section 3 presents an example of TC observed by the SWIM instrument. Section 4 presents a statistical analysis of the wave parameters characterizing the wave spectra. The results on the spectral shape of the directional and omni-directional spectra are presented in section 5. In section 6, a discussion is proposed to relate the different results presented in the previous sections. Finally, the conclusion is in section 7.

2 Data set and methods

2.1 Tropical cyclones data

TC parameters used in this study are taken from the International Best Track Archive for Climate Stewardship (IBTrACS) which combines TC best track data from 11 TC forecast centers all around the globe (Knapp et al., 2010, 2018). This database is recognized as the best source of information concerning TCs. The data set contains information about the storm time, position and category on one hand, and information about TC characteristics such as the maximum sustained wind, the minimum central pressure and the different wind radii on the other hand. TC characteristics used in this study are the maximum sustained wind speed (U_{max}), the radius of maximum sustained wind speed (R_{max}), and the displacement speed (V_t). These characteristics are available every 3 hours. Over the period of SWIM observations retained in this study (from May 2019 to September 2022), 134 TCs of category 1 to 5 occurred in the Northern Hemisphere. The CFOSAT mission provided observations in 67 of these TCs.

2.2 Wave data

The SWIM instrument is a wave scatterometer with six radar-beams rotating around the nadir axis at small incidences (close to 0°, 2°, 4°, 6°, 8°, 10°, respectively). Details on the measurement principle can be found in Jackson et al. (1985a), and the space-borne configuration with SWIM is detailed in Hauser et al. (2017).

Using the concept of real-aperture scanning radar, SWIM measures in all azimuth directions the signal modulations related to the slope of the long waves. The wave spectrum is estimated in each look direction from a Fourier analysis of the signal modulations (assumed to be linearly related to the slope of the long waves). The full directional spectrum is calculated (with an ambiguity of 180°) by combining observations covering 180° in azimuth. Wave parameters (such as dominant wavelength and direction) can then be estimated from the spectra. From the nadir beam observations, SWIM also provides the significant wave height $/Hs$), similarly to altimeter missions. In the version used here, this Hs measurement is used to normalize the directional spectral energy (as explained in Le Merle et al. (2021) their Equation 1, and as used in the operational near-real time processing since December 2020).

The data set corresponds to the L2P products provided by the AVISO+ French Data Center. They consist in directional spectra defined in 32 wavenumber bins from 0.013 rad/m and 0.28 rad/m and 12 direction intervals of 15° between 0° and 180°. The directional spectra are provided with an ambiguity in direction of 180°. Each spectrum is representative of an area of 90 km across-track and 70 km along-track called wave cell. The sampling is continuous along the satellite track and provides two spectra on each side of the nadir track. In the following, we only consider spectra obtained over the open ocean (without land or sea ice in the wave cell) and with valid data in each azimuth sector.

The validation of SWIM data has been the subject of several previous papers. In particular, comparisons on a point-by-point basis at the global scale using buoy and wave model data have been discussed by Hauser et al. (2021) and Le Merle et al. (2021). They proved the general good consistency of the mean wave parameters in cases of significant wave height larger than about 1.8 m, with smaller uncertainties on wave parameters when they are estimated from the 10° SWIM beam compared to the 6° and 8° beams. Therefore, in the present study we only use the spectra estimated from the 10° beam observations. Also, based on a statistical analysis per category of sea-state using buoy measurements, Xu et al. (2022) illustrate that for the conditions of SWIM acquisition chosen here (beam 10°), even in high sea-state conditions characterized by fully developed wind-sea or long swell as those encountered in the TCs, the distributions of wave energy with frequency and direction are very consistent with those observed with buoy data (see e.g. their Figures (2-f-i-l) and (5c-f-I)) and the spectral correlation coefficient between buoy and SWIM spectra is close to 1 (see e.g. their Figure 6(a)). In fact, the study by Xu et al. (2022), shows that the conditions where some non-linearity in the relation between wave slope and the measured signal modulations may alter the shape of the spectra and induce bias in the dominant wavelength are those of young wind seas, and large significant slope. As discussed later in Section 4, these are not the conditions that dominate the wave field in TCs. Finally, in the analysis presented in this paper, the spectral energy is normalized by the significant wave height Hs provided by the SWIM nadir beam (see Le Merle et al. (2021) their Equation 1). As several previous validations have assessed the very high consistency of Hs from the SWIM nadir observations compared to either altimeter missions or buoy measurements (e.g. Hauser et al., 2021; Tourain et al., 2021; Ye et al., 2021; Li et al., 2021), we are very confident in the spectral energy analyzed here.

We recall here that Hs is related to the directional ocean wave height spectrum ($F(k,\phi)$) by :

$$Hs = 4 \times \sqrt{\int \int_0^{\pi} F(k,\phi)\ k\ dk\ d\phi} \tag{1}$$

with k the wavenumber and ϕ the azimuth direction.

The wave products extracted from AVISO+ include additional wave parameters such as the wavelength and the direction of the dominant waves (λ_p and ϕ_p, respectively) estimated from the directional wave slope spectra expressed in wavenumber. Here, in order to analyze wave parameters similar to those already discussed in the literature on waves in TCs (e.g. Young, 2006; Tamizi & Young, 2020; Esquivel-Trava et al., 2015), we recalculated the dominant direction and the dominant wavelength from the directional wave height using the same approach as mention in the Product User Guide. The frequency directional wave height spectra were therefore converted from the wavenumber directional wave slope spectra provided in the SWIM products. Moreover, as indicated in Le Merle et al. (2021) and in Tourain et al. (2021), some of the directional wave height spectra have non-geophysical energy peaks at low wavenumbers/frequencies that can affect the calculation of the dominant frequency and direction. In order to attenuate this spurious energy, a 2D Gaussian filter is applied to smooth the directional spectrum before the calculation of the wave parameters. The estimated λ_p is obtained from the dominant frequency, f_p, using the dispersion relationship in deep water:

$$\lambda_p = \frac{g}{2\pi f_p^2} \tag{2}$$

with g the gravitational acceleration which is equal to 9.81 m/s^2.

As mentioned at the beginning of this section, the SWIM spectra are provided with a 180° ambiguity in the wave propagation direction. Therefore, the direction of the dominant waves can only be provided with an ambiguity of 180°. However, even if the wind and wave fields are complex in TCs, it is possible to remove this 180° ambiguity. Previous results in the literature showed that, under TCs conditions, the angle between the direction of the wind and the direction of wave propagation is always lower than 180°. This has been confirmed with buoy observations, and simulated wave spectra (e.g. Hu & Chen, 2011; Esquivel-Trava et al., 2015; Kudryavtsev et al., 2021b; Young, 2006). Therefore, to raise this 180° ambiguity on the SWIM wave spectra, we calculate the difference between the wind and the wave direction propagation and if this difference is higher than 180°, we add 180° (modulo 360°) to the direction of the dominant waves. Please note that this correction is only applied to estimate the direction of propagation of the dominant wave for each of the wave spectra obtained by SWIM.

Here, in order to analyze the development stage of the wave field around TCs, we calculated the inverse wave age (Ω), defined as classically as:

$$\Omega = \frac{U_{10} \cos(\phi_w - \phi_p)}{C_p} \tag{3}$$

with U_{10} the wind speed at 10 m height and ϕ_w the wind direction relative to the North. C_p is the wave phase velocity. The wind information is taken from the ancillary data available in the SWIM products. It is provided by the ECMWF atmospheric model 6-hours forecast collocated with the SWIM observations.

2.3 Methods

In this study we choose to focus our analysis on category 1 to 5 TCs according to the Saffir-Simpson scale. It means that the maximum sustained wind speed is at least 30 m/s, exceeding tropical storm and tropical depression intensity.

The purpose of this study is to investigate the impact of the TC characteristics on the distribution of the wave field. However, the wave field asymmetry varies according to the hemisphere with the highest waves on the right (left) side of the TC in the Northern (Southern) Hemisphere. In order to exclusively consider the TC impacts on the wave field, we decided to analyze the SWIM data crossing over TCs occurring only in the Northern Hemisphere. Every CFOSAT track passing within a distance of 4 R_{max} from the TC center and with a time difference of less than 1h30 is selected. Along these selected tracks, observations within 9 R_{max} are selected to perform the analysis.

This analysis has been carried out over more than a three-year period, between May 2019 and September 2022. During this period SWIM flew over 67 different TCs and provided 2360 ocean wave spectra in the Northern Hemisphere. However, we filtered out cases with Hs lower than 1 m and λ_p lower than 70 m (which represents less than 2.5% of the data (56 spectra)) because it was demonstrated that SWIM has some limitations in these situations (Le Merle et al., 2021). As TCs last for several days, it is not rare to have two or three flybys of a same event.

As mentioned in the introduction, several studies have shown that the displacement velocity of the TC has an impact on the wave field. Due to the displacement of the TC, the wind field can move forward with the waves it has generated and in certain conditions the waves remain under the action of strong winds for extended periods. In order to consider this process of extended fetch we choose to establish three classes of TCs based on the ratio of the maximum sustained wind speed to the displacement speed: U_{max}/V_t. The boundary of these classes are inspired by the numerical study of Kudryavtsev et al. (2021b). We choose the following classes: slow-moving TCs have $12 < U_{max}/V_t$; moderate speed moving TCs have $5 \leq U_{max}/V_t \leq 12$ and fast-moving TCs have $U_{max}/V_t < 5$.

Figure 1(a) shows the normalized histogram of SWIM observations according to U_{max}/V_t. The majority of SWIM observations are obtained in fast-moving TCs (48% of the SWIM spectra) whereas only 14% of the SWIM spectra have been obtained in slow moving TCs and 38% have been obtained in moderate speed TCs. It is interesting to note that all slow-moving TCs have displacement speed slower than 5 m/s whereas moderate speed TCs have $2 < V_t < 9$ m/s and fast-moving TCs have $V_t \geq 6.7$ m/s. Slow and moderate speed moving TCs have maximum wind speed between 30 m/s and 67 m/s whereas 94% of the observations in fast-moving TCs have been acquired under conditions with wind speed between 30 and 45 m/s. Therefore, even if the classes are established with the ratio U_{max}/V_t, the displacement velocity mainly controls the TC classification.

Figure 1(b) shows the normalized histograms of the SWIM observations according to the R_{max} for each classes. Despite the fact that most of the moderate speed TCs have R_{max} lower than 100 km, the distributions of R_{max} for each of the TC class overlap each other meaning that this characteristic is not impacted by the classification.

Recently, Kudryavtsev et al. (2021b) designed a 2D parametric model that can be used to forecast the main wave paramter under TC conditions. In this context they define a "true" criterion dividing TCs into two classes: fast or slow. This criterion has been established thanks to fetch and wave growth laws and is expressed as the ratio between the radius of maximum wind and the critical fetch: R_{max}/L_{cr} with the critical fetch expressed as:

$$L_{cr} = C_{cr} \times \frac{U_{max}^{-2}}{g\,(2V_t)^{-4}} \tag{4}$$

With C_{cr} a constant established thanks to the fetch laws. According to Kudryavtsev et al. (2021b), fast TCs correspond to $R_{max}/L_{cr} < 1$ and slow TCs correspond to $R_{max}/L_{cr} > 1$. Figure 1(c) shows the normalized distributions of the ratio between the maximum sustained wind speed and the displacement velocity of the TCs $\left(\frac{U_{max}}{V_t}\right)$ for cases with the

criterion R_{max}/L_{cr} greater and lower than 1 (in blue dotted line and in orange, respectively). In our data, cases with the criterion $R_{max}/L_{cr} < 1$ correspond to situations with U_{max}/V_t lower or equal to 5 and the distribution of the cases with the criterion $R_{max}/L_{cr} > 1$ correspond to situations with U_{max}/V_t higher or equal to 3.5. So, although the two distributions are overlapping between $3.5 \leq U_{max}/V_t \leq 5$, the two criteria are mutually consistent to classify TCs. This is because U_{max} and $V_t$also appear in R_{max}/L_{cr}, although with a different weight of V_t compared to that in our criterion. Furthermore, values of $R_{max}$are not really clearly related to any TC class according to U_{max}/V_t (see Figure 1(b)).

In order to compare the wave field observed by SWIM under TC conditions, the observations obtained in each TC of each class need to be combined in a same reference system. To do so, the SWIM observations are projected into a reference frame centered on the TC center with the frame upward direction aligned with the TC displacement direction. This reference frame is separated into four quadrants according to the center and to the displacement direction of the TC: the left front, right front, right rear and left rear quadrants. Moreover, the spatial scale is divided into three classes of radial distances normalized in terms of R_{max}: $0 \leq d/R_{max} < 3$, $3 \leq d/R_{max} < 6$ and $6 \leq d/R_{max} < 9$, with d the distance between the TC center and the SWIM observation.

Table 1 reports the number of ocean wave spectra obtained by SWIM for every TC class and for every class of radial distance. The numbers in brackets indicates the number of different TCs observed. Please note that, as the classification of the TCs is based on their characteristics which vary over time, it is possible that a TC observed twice appears in two different classes if its characteristics have changed between the two observations. Overall, the majority of observations was obtained for radial distances between 3 and 6 R_{max}, whereas the less sampled radial distances are those close to the TC center (up to 3 R_{max}).

In the following sections, the evolution of the wave parameters, the shape of the mean directional and omni-directional spectra are analyzed in the four quadrants and in the three classes of radial distances for the three TC classes.

3 Case study - Hurricane Douglas

The hurricane Douglas occurred in the Western Pacific between the 20^{th} and the 30^{th} of July 2020 and has been observed by the CFOSAT mission the 24^{th} of July at 4:15 a.m. At this time, according to the IBTrACS data, the radius of maximum sustained wind speed was 27 km, the maximum sustained wind speed was 59 m/s and the displacement velocity was about 8 m/s. When SWIM flew over the hurricane Douglas, it was a moderate speed moving tropical cyclone according to our classification ($U_{max}/V \sim 7$). Figures 2(a,b) show the evolution of Hs and λ_p along the SWIM track projected in the TC reference frame. The arrows represent the wind and the dominant wave propagation direction, respectively. The direction of the dominant waves has been corrected according to the method explained in section 2.2. The SWIM track is presented in the tropical cyclone reference frame with the hurricane Douglas in the middle of the map and the propagation direction of the hurricane aligned with the upward direction.

According the the ECMWF model, in the right front quadrant, the wind direction is oriented towards the North-East direction relative to the TC propagation direction. Within the area between the TC center and 9 R_{max}, the wind direction varies rapidly in space, rotating around the TC center (Figure 2(a)). The highest values of Hs are on the right side of the hurricane, whereas the smallest values of the dominant wavelengths are on the left side of the hurricane Douglas track indicating an asymmetry of both wave parameters (Figure 2(a-b)). Moreover, in the right quadrant, up to 500 km from the TC center (dashed line circle), the dominant wave direction is almost aligned with the TC direction propagation whereas in the left quadrant the dominant direction is perpendic-

ular to the propagation direction of the hurricane. One can also notice a variation of about 180° of the wave direction from one spectrum to the other in the left quadrant which is due to the limitation of the ambiguity correction.

Figures 2(c-d) show two examples of wave slope directional spectra obtained at a distance of approximately 4 R_{max} on the left and on the right side of the TC, respectively. The spectrum obtained on the left side of the TC shows two energy peaks corresponding to two wave systems with similar dominant wavelength (Figure 2(c)). The most energetic system is aligned with the wind direction. The spectrum obtained on the right side of the TC shows different features from the other one, with only one wave system which is aligned with both the wind and the TC propagation direction (Figure 2(d)).

4 Statistical analysis of wave parameters

In this section we present a statistical analysis of the wave field parameters estimated from the SWIM data. Wave parameters are analyzed for the three TC classes, in each of the four quadrants and for the three classes of radial distances ($0 \leq d/R_{max} < 3$, $3 \leq d/R_{max} < 6$ and $6 \leq d/R_{max} < 9$).

Figure 3 shows the statistics of the significant wave height. The three different panels correspond to the TC classes: slow (left panel), moderate speed (middle panel) and fast (right panel). In each panel, the distributions are shown as boxplots with, from left to right, the distributions of the left front, right front, right rear and left rear quadrant respectively. The light, medium and dark blue colors stand for the distance ranges ($0 \leq d/R_{max} < 3$, $3 \leq d/R_{max} < 6$ and $6 \leq d/R_{max} < 9$, respectively). The solid box represents the interquartile range (IQR), i.e. the distance between the first and third quartile. The whiskers delimit the ±1.5 IQR interval, and the circle symbols show the values outside this range. The horizontal solid (respectively dotted) line represents the median (respectively mean) value.

One common feature for all the TC classes and all quadrants is that Hs decreases from the near range (light blue) to the far range (dark blue). A significant asymmetry is observed in all TCs at distances up to 6 R_{max}, but the maxima are not in the same quadrant according to the TC class: at distances less than 3 R_{max}, the highest mean Hs (≈7.5 m) are observed in the right front quadrant for moderate speed moving TCs, whereas for slow and fast moving TCs, they are found in the left front and right rear quadrant, respectively. Overall, there is a marked difference in the Hs asymmetry between fast, slow and moderate speed TCs meaning that the relative displacement speed of the TC has a significant impact on the asymmetry of Hs. This is consistent with the simulations carried out by Kudryavtsev et al. (2021b) - see their Figure 7. Furthermore, the highest values of Hs are observed in fast moving TCs, which is consistent with the results of Collins et al. (2021) who found the maximum values of Hs increase with the TC displacement speed.

Figure 4 shows the distributions of the dominant wavelengths (λ_p) estimated from the wave height SWIM spectra in frequency as explained in section 2.2. The distributions of the dominant wavelengths are more homogeneous within the TCs than the significant wave height in the sense that the average values stay between 200 m and 280 m. There is almost no case with peak wavelength shorter than 100 m and the maximum value of all IQR is lower than 350 m. However, a slight asymmetry is visible: longer wavelengths are observed in the left front quadrant for slow-moving TCs and in the right front quadrant for the moderate speed TCs (at least at distances up to 6 R_{max}). In opposite, there is no clear trend of asymmetry of λ_p in fast moving TCs.

Figures 5(a-b) show fields of wind and dominant wave direction. Slow and moderate speed TCs have been superposed on the same panel in Figure 5(a) whereas results for the fast-moving TC conditions are illustrated in Figure 5(b). The black arrows in-

dicate the direction towards which the wind is blowing and the red arrows represent the propagation direction of the dominant waves. All arrows are plotted in the TC reference frame (the TC propagation direction is oriented towards the top of the page). The length of the black arrows corresponds to the wind speed at 10-m height and the length of the red arrows is proportional to the dominant wavelength. We recall that the wind information is from the ECMWF model forecast provided in the SWIM product files. In these figures, the dominant wave direction have been corrected from the 180° ambiguity as explained in section 2.2. To make the maps of Figure 5 more readable, all the directions of wind and waves have been average in space on a regular grid with a resolution of 0.25 R_{max}.

The wind direction from ECMWF is found consistent with the typical wind direction field analyzed with buoy observations by (e.g. Hu & Chen, 2011; Esquivel-Trava et al., 2015). It is notable that the waves are never aligned with the wind direction, except very close to the TC center. In the main part of the right front quadrant, the dominant waves propagate along the TC trajectory, whereas the wind travels to the left of the direction of the TC displacement. For slow and moderate speed TCs (Figure 5(a)) the composite map is in qualitative agreement with the one established by Esquivel-Trava et al. (2015)for distances up to 10 R_{max} from buoy observations in 14 hurricanes: the smallest angles between wind and waves is found in the forward quadrants (especially the right front quadrant) and the largest values are at the rear where wind direction is often opposite to the waves (angles large than 90°).

In fast-moving TCs (Figure 5b), the wind and wave fields are more confused. This may be due either to the fact that under fast-moving TCs the wind field is less homogeneous than in slow or moderate speed moving TCs or that the forecast model have difficulties to correctly represent the wind field in these cases. Additionally, the more confused wave directions may be due to the presence of several wave systems as it will be discussed in the next section. This wind and wave direction fields indicate that in fast-moving TCs both the wind and the wave fields are more complex than in slow and moderate speed TCs.

Figures 6(a-c) show the distributions of the angles between the direction of the dominant waves and the direction of the wind in slow, moderate speed and fast-moving TCs, respectively. These distributions have been obtained by first removing the 180° ambiguity on the wave direction, assuming that the waves always propagate to the right side of the wind direction (see Section 2.2). This explains why the scale of Figures 6(a-c) is between 0° and 180°. The shaded area in these plots highlight values greater than 90°, corresponding to cases where the wind blows with a component opposite to the wave direction. From these figures, it is clear that there are numerous conditions where the wind does not blow in the wave direction: for example it occurs under fast TCs, at all distances, and for the other classes of TCs, at distances greater than 6 R_{max}. In contrast, in TC of slow and moderate speed, the wind has a component aligned with the waves for a majority of samples in the right quadrants, where the angle between wind and waves is also the smallest. We can expect that the wind efficiently forces the wave growth only when it has a component aligned with the waves, provided that the ratio of wind speed to phase velocity (also called inverse wave age Ω) is greater than 0.83 (see e.g. Donelan et al. (1985)). Figures 6(d-f) show this inverse wave age estimated by accounting for the angle between wind and waves (parameter Ω Eq.3), whereas Figures 6(g-i) show the inverse wave age estimated without accounting for the angle between wind and waves (noted U_{10}/C_p).

It is clear from Figures 6(d-f) that there is only a small number of samples where Ω is larger than 0.83 (that is, condition of non-fully developed waves) whatever is the TC class; the fast moving TCs are however more favorable for this condition. In contrast, from Figures 6(g-i), we can see that if U_{10}/C_p is chosen as the inverse wave-age parameter, then the number of samples with non-fully developed waves is quite large, in particular at small distances (less than 3 R_{max}). Thus, it appears that it is the angle be-

tween wind and waves that governs the effective wave age, and that this latter is not in favor of an efficient wave growth by wind energy input.

Figures 6(d-f) also show a large number of samples with negative values of Ω (corresponding to cases with an angle between wind and waves larger than 90°). In these cases at least, it is evident that wind is not an efficient mechanism for the wave growth and that other mechanisms must be invoked to explain the maintenance of large significant wave heights. Tamizi et al. (2021) have shown with numerical simulations that indeed the non-linear interactions between waves dominate the wave energy source terms when the directional spectra are spread in direction, thus confirming the intuition of Young (2006). But this simulation concerns only two cases of TC with slow to moderate displacement speed. We will come back to this discussion in the next sections.

In Figures 6(g-i), it is also notable that for almost cases, U_{10}/C_p decreases with distance. We checked that this variation is mainly due to the decrease of wind speed with distance rather to increase in C_p. This variation with distance is however not anymore visible when Ω is considered as the inverse wave age parameter.

By combining the results presented above on the main wave parameters in the three classes of TCs, the main conclusions are the following. First, the highest significant wave heights are observed at distances less than 3 R_{max} and in the right front quadrant of moderate speed TCs, in the left front quadrant of slow TCs and in the right rear quadrant of the fast TCs. This occurs whilst the inverse wave age Ω (which takes into account the angle between wind and waves), corresponds to a large majority of cases of fully developed waves ($\Omega < 0.83$), even if the along-wind inverse wave age U_{10}/C_p indicates non-fully developed waves.

In the cases of moderate speed TCs, the highest significant wave height occurring in the right front quadrant at distances less than 3 R_{max} (IQR≈[6-9] m) are associated with the smallest angles between wind and waves (IQR=[40-80]°) , and with the longest dominant wavelengths (IQR≈[220-300] m), indicating that wind input may still be efficient for wave growth is spite of low Ω values. The wave growth by the wind is probably facilitated by the fact that the waves remain for a long time under the wind forcing in these conditions of TC with moderate displacement speed, as shown by the simulations of Kudryavtsev et al. (2021b).

For the slow-moving TCs, the highest values of Hs occurring in the left front quadrant at distances less than 3 R_{max} (IQR≈[7-9] m) are associated with long wavelengths (IQR≈[200-280] m), large angles between wind and waves (sometimes even with the wind blowing against the waves), and wave age values corresponding to fully developed waves. In these conditions, it is rather unlikely that growth by the wind explains the maximum values of Hs.

For the fast-moving TCs, the highest values of Hs occurring in the right rear quadrant at distances less than 3 R_{max} (IQR≈[6-10] m) are associated with a broad distribution of the angle between wind and dominant waves (IQR [25-150]°), and with wavelengths about IQR≈[200-350] m. We suspect that this is because wave spectra have multiple peaks of similar energy so that the dominant waves are found at directions and wavelengths which are not very stable in space. This point is further discussed in section 5.2.

Overall, the asymmetry of Hs and of λ_p between the four quadrant decreases with the distance from the center of the TC.This is the most visible in fast-moving TCs and this is consistent with the numerical results of Kudryavtsev et al. (2021b).

5 Spectral shape analysis

5.1 Directional spectrum

In this subsection mean wave height directional spectra are analyzed in all quadrants and distance ranges for slow, moderate and fast-moving TCs (Figures 7, 8, 9, respectively). Before calculating the mean spectra, they were rotated so that the 0° direction of every spectrum corresponds to the displacement direction of the TC.

It is worthwhile to note that generally, the spectra show complex and variables features with either mono-modal, multi-modal features or important spread in the energy depending on the position within the TC and on the TC class. In order to differentiate in our discussion mono-modal to multi-modal features in direction, we consider a that a secondary peak is significant when its maximum energy reaches at least 45% of the maximum energy of the entire spectrum.

In slow-moving TCs (Figure 7), in the entire left front quadrant the wave field is essentially mono-modal and the waves propagates at ∼45° to the left of the displacement direction of the TC. In the left rear quadrant the spectrum close to the center of the TC is mono-modal with a significant directional spreading of the energy. While the distance from the TC center increases the energy spreads in direction leading to a bi-modal spectrum at distances larger than 6 R_{max} with two peaks of similar maximum energy and similar dominant wavelengths of approximately 170 m and 200 m. In the right front quadrant and at distances larger than 3 R_{max}, the dominant direction is aligned with the displacement direction of the TC. In the right rear quadrant, the spectra are bi-modal with similar dominant wavelengths at distances less than 3 R_{max}. The difference between the dominant wavelengths increases with the distance from the TC center.

For the moderate speed class (Figure 8), mono-modal spectra with limited spread of energy in direction are observed in the right front quadrant, with the wave propagation clearly aligned with the displacement direction of the TC. There are also mono-modal spectra in the left front quadrant and the waves propagate with an angle of ∼45° on the left of the displacement direction of the TC as in slow moving TCs. In the left rear quadrant the mean spectrum at distances less than 3 R_{max} is also mono-modal but its energy spreads in direction. While the distance from the TC center increases; the mean spectra become bi-modal with the secondary peak less energetic than the dominant one. In the right rear quadrant, the energy spreads in direction while the distance from the TC center increases leading to a bi-modal spectrum at distances larger than 6 R_{max}.

In fast-moving TCs (Figure 9), the mean spectra in both left quadrants are either multi-modal or significantly spread in direction. In opposite, in both right quadrants, the mean spectra are mono-modal, except the one at distances larger than 6 R_{max} in the right front quadrant which is bi-modal with a peak of energy close to 500 m in wavelength. In the entire right front quadrant the dominant waves are aligned with the displacement direction of the TCs whereas in the right rear quadrant, it is only the case for the mean spectrum at distances less than 3 R_{max}.

5.2 Omni-directional spectrum

Figure 10 presents the omni-directional spectra obtained in situations of moderate speed TCs as a function of the normalized frequency (f/f_p) where f_p is the dominant frequency of the waves. The energy density is also normalized by the total energy of the omni-directional spectrum. The name of the quadrants are indicated in the top right corner of each panel. In all quadrants, the trend of the mean spectra (black squares) show a continuous decrease of energy at frequencies higher than f_p. At $f/fp > 2$, one can notice that the dispersion of the spectral energy becomes more important especially for observations obtained at more than 3 R_{max}. The mean and standard deviation of

the spectral energy (black squares and yellow error bars in Figure 10, calculated over all spectra present in each quadrant, are clearly impacted by this dispersion.

In the following we show and discuss the mean normalized spectra calculated for each distance range in each quadrant for the moderate speed TCs (Figure 11). The spectral parametric form estimated by Young (2006) is also plotted in each quadrant. This model is an adaptation of the JONSWAP (Donelan et al., 1985) spectral model estimated from buoy observations in 9 hurricanes along the Australian coasts. We calculated this parametric model by using the average wind speed (U_{10}) (from the ECMWF model co-localized with the SWIM spectra) and the mean dominant frequency of all the SWIM spectra obtained in each quadrant. We also checked that these mean "Young2006" spectra are close to the mean spectra obtained by averaging all the "Young2006" spectra corresponding to all observations.

Figure 11 indicates that on the right-side of the dominant frequency ($f/f_p > 1$) the mean spectra are mono-modal in all quadrants, at all distance ranges. In all quadrants, we can also see a secondary energy peak at lower frequencies (at about $f/f_p \sim 0.5$). This peak indicates the presence of at least a secondary wave component at a lower frequency than the dominant frequency as it is illustrated by the turquoise curve in Figure 12 which show an example of a wave height spectrum obtained under moderate speed TC condition, at a distance larger than 6 R_{max}. This spectrum exhibits two energy peaks: the dominant one at $f/f_p = 1$ and another one at $f/f_p \approx 0.7$ which can be assimilated to a swell component.

Coming back to Figure 11, observations obtained close to the TC center ($d/R_{max} < 3$), the decreasing trend of the normalized energy with the normalized frequency does not change significantly from one quadrant to another and it is very close to the parametric model proposed by Young (2006). On the contrary, at largest distance from the TC center, this trend differs significantly from the Young's model (Young, 2006) with a more gentle decrease of the normalized energy with f/f_p, especially in the left front and right rear quadrants. In the individual normalized spectra used to obtain Figure 11, f_p generally corresponds to a low frequency peak which does not change significantly with position within the TCs whereas depending on the quadrant and the distance, the frequency of the secondary peak (wind sea) may be more variable. In consequence, after applying the averaging process to obtain the mean spectra of Figure 11, this leads for certain quadrants and distances, to an increase of energy at $f/f_p > 1.5$ to 2. This phenomenon is illustrated in Figure 12 by the orange wave spectrum where a secondary peak of energy appears at $f/f_p \approx 2.3$. In these conditions, the omni-directional spectra are normalized with respect to the dominant frequency of the swell whereas the wind-sea part may have a variable dominant frequency and therefore increases the energy at high frequencies ($f/f_p > 1$).

In case of slow-moving TCs, the conclusions are similar to the ones discussed just above for the moderate speed cases. However, in fast-moving TCs, the trend of the mean spectra is less steep than the trend of the parametric model proposed by Young (2006) in each quadrant and in each distance ranges. This is explained by the presence of several wave systems since, as we mentioned in section 5.1, in fast-moving TCs, for almost all quadrants and distances, directional spectra exhibit mixed-sea conditions, or a significant spreading of the energy.

This analysis of the shape of the spectra shows that it is important to sort the data according to both the distance to the center and the relative speed of the TC. Indeed, the slope of the mean spectrum is different depending on whether the spectra are averaged over the entire quadrant (black squares in Figure 10) or over a particular distance range such as in Figure 11.

Similarly to the study of Tamizi and Young (2020) we also estimated the n factor with the omni-directional SWIM spectra. However, because of the possible impact of mixed-sea on its estimation, we decided to calculate the n factor only for slow and moderate speed TCs, for observations obtained close to the TC center ($d < 3R_{max}$). This factor is estimated between $1.5f_p$ and $3.5f_p$ as shown in Figure 12 and in order to account for the limitations of the SWIM detection, we filtered out the energy at frequency higher than 0.2 Hz which corresponds to 40 m of wavelength. Furthermore, we kept the obtained n value only if its estimation is based on more than 5 points. However, as discussed previously, at distances larger than 3 R_{max}, there are some cases of mixed-seas that can bias the estimation of n. Therefore, to avoid this limitation, the n factor has been calculated for observations acquired at distances less than 3 R_{max} in slow or moderate speed TCs.

Figure 13 shows the n factor as a function of U_{10}/C_p. As in Tamizi and Young (2020), we obtained an important scatter and there is no an obvious relationship between this factor and the U_{10}/C_p. So, conclusions obtained by Tamizi and Young (2020) are confirmed by the SWIM data but only for TC of slow and moderate speed. However, the mean value obtained with the SWIM data is lower than the one obtained by Tamizi and Young (2020) (3.53±0.45 and 4.68, respectively) and lower than the value obtained by Donelan et al. (1985).

Finally, the non-dimensional relationships between wave energy and dominant frequency are analyzed. Figures 14(a-c) represent the variation of the non-dimensional energy ϵ with the non-dimensional frequency ν for slow, moderate and fast-moving TCs, respectively. Non-dimensional energy and frequency were determined as:

$$\nu = \frac{f_p U_{10}}{g} \tag{5}$$

$$\epsilon = \frac{g^2 E_{tot}}{U_{10}^4} \tag{6}$$

with E_{tot} the total energy of the wave spectrum. The black solid line represents the linear fit for the data obtained in each class, whereas the black dashed line represents the fetch-limited relationship estimated by Donelan et al. (1985). It is interesting to note that for each class, a clear non-dimensional relationship is found when we combined all observations obtained at all distances. Observations obtained at less than 3 R_{max} from the TC center (light blue circles) behave similarly between all classes and are close to the values provided by Donelan et al. (1985) relationship.

6 Discussion

The analysis of the SWIM data performed by separating the TCs in different classes according to their relative speed allows us to highlight that the wave field is different from one class to another. According to our results, we find as in Young (2006) or Shi et al. (2021) that Hs is higher on the right front quadrant of the TCs, but this is true only in situation of moderate speed TCs. In case of slow-moving TCs, the highest Hs are observed in the left front quadrant, whereas in fast-moving TCs the highest Hs are observed in the right rear quadrant.

The impact of the TC relative displacement speed on Hs field is in agreement with the model results of Kudryavtsev et al. (2015, 2021a, 2021b), both with the physically-based model which treats the wave parameters evolution along wave rays in a Lagrangian reference frame, and with the fully parametric model based on the TC parameters. It is also interesting to compare our statistical results with the analysis recently proposed by Yurovskaya et al. (2022) of the cyclone Goni (2020). In this study the authors compared SWIM observations to model results obtained from the two approaches developed by Kudryavtsev et al. (2021a, 2021b), when Goni had a relative displacement velocity

corresponding, according to our classification, to the moderate speed class ($U_{max}/V_t \sim 9$). Model results shown by Yurovskaya et al. (2022) -their Figure 4- are qualitatively consistent with our statistical results for the moderate class: largest significant wave height close to the TC center and in the right front quadrant, longest (resp. shortest) dominant wavelengths in the right front (resp. right rear quadrant).

It is also interesting to compare our results on the directional spectra with those obtained in the cyclone Bonnie (1998), which is probably the most extensively documented TC in the literature concerning the waves thanks to the analysis of airborne measurements with the Scanning Radar Altimeter Wright et al. (2001); Hwang and Walsh (2018) and associated wave modeling Moon et al. (2003). According to our classification, at the time of the airborne measurements when Bonnie was over the open ocean, it was a moderate speed TC ($U_{max}/V_t \sim 10$). Qualitatively, in similar conditions,the correspondence between our statistical results (Figure 8) at $d/R_{max} < 3$) and those from the above-mentioned authors (e.g. Figure 3 of Hwang and Walsh (2018) for $d < 200$ km, i.e d/R_{max} up to 2.7 with R_{max}= 74 km) is very good in terms of dominant wave directions, dominant wavelengths and shape of the spectra (mono- or multi-modal). This allows to generalize some of the conclusions previously proposed in the literature.

In particular, one clear feature is that in the right front quadrant, directional spectra are mono-modal in moderate speed TCs with waves propagating along the displacement direction of the TC. In contrast, in the right front quadrant of slow and fast TCs, the energy is more spread in direction and wavelength and the dominant waves are not always aligned with the cyclone track. In the left front quadrant, for all TC classes, the dominant waves propagate towards the NW of the TC track and at significant angle from the wind direction.

In the left rear quadrant, spectra for moderate speed TCs have a clear dominant wave direction along SE direction relative to the TC and a secondary maximum along the W-E axis whereas in slow and fast-moving TCs, the shape of the mean spectra is more complex with multi-modal spectra and varying dominant wave direction with the distance from the TC center. In the right rear quadrant, the mean spectra are multi-modal in moderate and slow TC classes as well as in fast TCs (at least close to the center), with varying dominant wave direction propagation according to the TC class.

In their study, Esquivel-Trava et al. (2015) calculated composite directional spectra per quadrants by averaging individual spectra from 0 to 10 R_{max} from 14 cyclones. Because no distinction was made in their case with respect to the cyclone displacement speed nor with the distance from the center, the comparison is not straightforward. However, in the two right quadrants and in the left front quadrant their spectra are similar to our mean spectra obtained under moderate speed TC conditions with the direction of the dominant waves aligned with the displacement direction of the TC in the right front quadrant. The tendency to have more spread in the energy distribution in both left and right rear quadrants is also consistent with our findings.

As mentioned in section 4, the effective inverse wave age Ω (which takes into account the phase speed of the dominant waves and the angle between wind and these dominant waves) does not seem an appropriate parameter to characterize the continuous growth of waves. Indeed, Ω corresponds almost everywhere to fully developed waves (Ω smaller than 0.83), mainly due to the important angle between wind and waves. So, we have to speculate that either the wind input remains efficient even in cases when dominant waves are not aligned with the wind or, as suggested by Young (2006), that another mechanism such as the 4-waves non-linear interactions plays an important role to maintain the waves under an efficient growing stage. According to Young (2006), and Tamizi and Young (2020), for wave spectra at distances of about 3 R_{max}, a smooth transition in energy occurs between the swell (remotely generated) and locally generated wind-sea. They suggest that this could be the signature of efficient non-linear wave-wave interactions that

could explain the absence of bimodality in the omni-directional spectra. This intuition was later verified by Tamizi et al. (2021) by evaluating, for two cases of TC (slow and moderate speed according to our classes) the different source and sink terms of the wave growth equation in a numerical wave model. They found that except in the right front quadrant where the wind input remains efficient for wave growth over all wave frequencies, the non-linear interactions play a major role in redistributing energy for spectra in the other quadrants, i.e. when the angle between wind and dominant wave is large. In absence of numerical modeling (which is out of the scope of this paper), it is not possible to firmly assess these conclusions with our observations. However, our results in the same conditions as those studied by Tamizi et al. (2021), i.e. slow and moderate cases and distances less than 6 R_{max} seem to support these conclusions.

The behavior of the omni-directional spectra also shows similarities but also some differences with respect to previous results. In fact, clear similarities with Young (2006) and Tamizi and Young (2020) are found when the individual spectra are mono-modal in frequency. This occurs close from the TC center in slow and moderate speed TCs but not in fast-moving TCs. The systematic presence of multi-modal spectra either far from the TC center or in fast-moving cases induce an estimation of the trend with the normalized frequency much less steep than in the above-mentioned reference. It has to be noted that spectra illustrated in Young (2006), and Tamizi and Young (2020) only refer to observations close to the TC center and probably to TC with slow to moderate speed. Our results, which cover a large range of distances and TC classes, indicate that the similarity with the laws of wind-waves under fetch-limited conditions holds only at less than 3 R_{max} in slow and moderate speed TCs.

Surprisingly, concerning the non-dimensional relationship between ν and ϵ, we find a relationship which is consistent with the fetch-limited relationship, whatever is the TC class even if samples far from the TC center are considered. This result is surprising because far from the center the wave field is characterized by multi-modal spectra with contributions of both swell and wind-sea with generally swell energy dominating. But the slope of the relationship ν and ϵ seems to remain the same for all ranges of ν either above 0.13 (wind waves dominating) or less than 0.13 (swell dominating). This confirms the results of Tamizi and Young (2020) and extends them to the cases of fast moving TCs. Thus, in TCs this self-similarity law between non-dimensional frequency and non-dimensional energy seems to hold even in mixed sea conditions.

7 Conclusions and perspectives

SWIM data have been analyzed in TC conditions over more than 3 years (May 2019-September 2022) in the Northern Hemisphere. The objective of this study was to characterize the impact of the TC features on the wave field. Several studies of the SWIM data at the global scale allow us to target the strengths and the limitations of the instrument (Hauser et al., 2021; Le Merle et al., 2021) and confirmed that the limitations of SWIM were limited in TC situations.

Thanks to the IBTrACS data we have established three TC classes based on the maximum sustained wind speed and on the displacement velocity. After collocating the SWIM data with the TC and referencing them in a coordinate frame centered on the TCs, we analyzed the distributions of the wave parameters and the spectral shape as a function of the quadrant and the distance between the observations and the center of the TC.

The analyses of the wave parameters indicate that there is an asymmetry of Hs and of the dominant wavelength (λ_p). This asymmetry varies with the TC class, and the maximum values observed are obtained in the right front quadrant in moderate speed TCs and in the right rear quadrant in fast moving TCs.

We also calculated mean directional spectra for each TC class, each quadrant and each distance. It appears that the spectral shape varies according to these different classes of observations. In moderate and slow-moving TCs, close to the TC center, the wave spectra tend to be mono-modal whereas far from the TC center and in fast moving TCs (especially in the left side), the spectra tend to become bi- or even multi-modal.

We have compared mean omni-directional spectra to a parametric model proposed by Young (2006) which generalizes the JONSWAP form in case of TCs. In slow and moderate moving TCs, close to the center, omni-directional spectra present consistencies with the "Young2006" spectrum whereas far from the TC center and in fast-moving TCs, the agreement is less satisfying. This can be partly explained by the presence of mixed-sea in which the swell is dominant.

Because of these situations of mixed-sea impact significantly the shape of the normalized omni-directional spectra, the n factor was discussed only for spectra in slow and moderate speed TCs, close to the TC center. It appears that the mean value of n obtained in these situations is close to the one obtained by Donelan et al. (1985) in fetch limited conditions. As previously shown by Tamizi and Young (2020), there is no obvious relationship between this n factor and the inverse wave age.

We also analyzed the relationship between the non-dimensional frequency and the non-dimensional energy from the SWIM spectra. These non-dimensional laws are verified but with a slope smaller than the one obtained by Donelan et al. (1985) in fetch-limited conditions. This smaller slope is also find in the numerical simulations of Tamizi et al. (2021).

Overall, from an analysis over 67 TCs, we confirm features already been mentioned in the literature such as the asymmetry of the wave field with higher waves in the right front quadrant and a spectral shape that have similarities with the fetch-limited parametric models. But, we also show that the TC characteristics, in particular its relative displacement speed, have an impact on the wave field. In particular, under fast-moving TCs none of these features could be evidenced.

8 Open Research

The SWIM data set used here corresponds to the files reprocessed in version 5 and made available by CLS on the ftp server of AVISO+ (ftp-access.aviso.altimetry.fr/, directory /cfosat/swim_l2p_box_nrt) accessible to anyone after registration.

The IBTrACS data used in this study correspond to the last 3 years file with reprocessed data in version 4 (IBTrACS.last3years.v04r00.nc). Data are available here:`https://doi.org/10.25921/82ty-9e16`. The data have been downloaded on the 9th of August 2021.

Acknowledgments

The authors would like to thank all the CFOSAT teams from CNES, CNSA, NSOAS for their involvement in the different stages in the mission and the CLS team for their work on the reprocessing of the L2 products.

References

Aouf, L., Hauser, D., Chapron, B., Toffoli, A., Tourain, C., & Peureux, C. (2021). New directional wave satellite observations: Towards improved wave forecasts and climate description in southern ocean. *Geophysical Research Letters*, *48*(5), e2020GL091187. Retrieved from `https://agupubs.onlinelibrary.wiley.com/doi/abs/10.1029/2020GL091187` doi:

https://doi.org/10.1029/2020GL091187

Bowyer, P. J., & MacAfee, A. W. (2005). The theory of trapped-fetch waves with tropical cyclones—an operational perspective. *Weather and Forecasting*, *20*(3), 229 - 244. Retrieved from `https://journals.ametsoc.org/view/journals/wefo/20/3/waf849_1.xml` doi: 10.1175/WAF849.1

Chen, S., Rutgersson, A., Yin, X., Xu, Y., & Qiao, F. (2020). On the first observed wave-induced stress over the global ocean. *Journal of Geophysical Research: Oceans*, *125*(12), e2020JC016623. Retrieved from `https://agupubs.onlinelibrary.wiley.com/doi/abs/10.1029/2020JC016623` doi: https://doi.org/10.1029/2020JC016623

Collins, C., Hesser, T., Rogowski, P., & Merrifield, S. (2021). Altimeter observations of tropical cyclone-generated sea states: Spatial analysis and operational hindcast evaluation. *Journal of Marine Science and Engineering*, *9*(2). Retrieved from `https://www.mdpi.com/2077-1312/9/2/216` doi: 10.3390/jmse9020216

Donelan, M. A., Hamilton, J., Hui, W. H., & Stewart, R. W. (1985). Directional spectra of wind-generated ocean waves. *Philosophical Transactions of the Royal Society of London. Series A, Mathematical and Physical Sciences*, *315*. doi: 10.1098/rsta.1985.0054

Esquivel-Trava, B., Ocampo-Torres, F. J., & Osuna, P. (2015). Spatial structure of directional wave spectra in hurricanes. *Ocean Dynamics*, *65*, 65-76. doi: 10.1007/s10236-014-0791-9

Fan, Y., Hwang, P., & Yu, J. (2020). Surface gravity wave modeling in tropical cyclones. In K. S. Essa, M. D. Risio, D. Celli, & D. Pasquali (Eds.), *Geophysics and ocean waves studies* (chap. 6). Rijeka: IntechOpen. Retrieved from `https://doi.org/10.5772/intechopen.93275` doi: 10.5772/intechopen.93275

Hauser, D., Tison, C., Amiot, T., Delaye, L., Corcoral, N., & Castillan, P. (2017, May). Swim: The first spaceborne wave scatterometer. *IEEE Transactions on Geoscience and Remote Sensing*, *55*(5), 3000-3014. doi: 10.1109/TGRS.2017.2658672

Hauser, D., Tourain, C., Hermozo, L., Alraddawi, D., Aouf, L., Chapron, B., ... Tran, N. (2021). New observations from the swim radar on-board cfosat: Instrument validation and ocean wave measurement assessment. *IEEE Transactions on Geoscience and Remote Sensing*, *59*(1), 5-26. doi: 10.1109/TGRS.2020.2994372

Hell, M. C., Ayet, A., & Chapron, B. (2021). Swell generation under extra-tropical storms. *Journal of Geophysical Research: Oceans*, *126*(9), e2021JC017637. doi: https://doi.org/10.1029/2021JC017637

Hu, K., & Chen, Q. (2011). Directional spectra of hurricane-generated waves in the gulf of mexico. *Geophysical Research Letters*, *38*(19). Retrieved from `https://agupubs.onlinelibrary.wiley.com/doi/abs/10.1029/2011GL049145` doi: https://doi.org/10.1029/2011GL049145

Hwang, P. A., Fan, Y., Ocampo-Torres, F. J., & García-Nava, H. (2017). Ocean surface wave spectra inside tropical cyclones. *Journal of Physical Oceanography*, *47*(10), 2393 - 2417. Retrieved from `https://journals.ametsoc.org/view/journals/phoc/47/10/jpo-d-17-0066.1.xml` doi: 10.1175/JPO-D-17-0066.1

Hwang, P. A., & Walsh, E. J. (2018). Propagation directions of ocean surface waves inside tropical cyclones. *Journal of Physical Oceanography*, *48*(7), 1495 - 1511. Retrieved from `https://journals.ametsoc.org/view/journals/phoc/48/7/jpo-d-18-0015.1.xml` doi: 10.1175/JPO-D-18-0015.1

Jackson, F. C., Walton, W. T., & Baker, P. L. (1985a). Aircraft and satellite measurement of ocean wave directional spectra using scannig-beam microwave radars. *Journal of Geophysical Research*, *90*(C1), 987–1004. doi:

0148-0227/85/004C-1190$05.00

Knapp, K. R., Diamond, H. J., Kossin, J. P., Kruk, M. C., & Schreck, C. J. (2018). *International best track archive for climate stewardship (ibtracs) project, version 4. [ibtracs.last3years.v04r00.nc]* [dataset]. NOAA National Centers for Environmental Information. Retrieved from https://doi.org/10.25921/82ty-9e16 doi: 10.25921/82ty-9e16

Knapp, K. R., Kruk, M. C., Levinson, D. H., Diamond, H. J., & Neumann, C. J. (2010). The international best track archive for climate stewardship (ibtracs): Unifying tropical cyclone data. *Bulletin of the American Meteorological Society*, *91*(3), 363 - 376. Retrieved from https://journals.ametsoc.org/view/journals/bams/91/3/2009bams2755_1.xml doi: 10.1175/2009BAMS2755.1

Kudryavtsev, V., Golubkin, P., & Chapron, B. (2015). A simplified wave enhancement criterion for moving extreme events. *Journal of Geophysical Research: Oceans*, *120*(11), 7538-7558. Retrieved from https://agupubs.onlinelibrary.wiley.com/doi/abs/10.1002/2015JC011284 doi: https://doi.org/10.1002/2015JC011284

Kudryavtsev, V., Yurovskaya, M., & Chapron, B. (2021a). 2d parametric model for surface wave development under varying wind field in space and time. *Journal of Geophysical Research: Oceans*, *126*(4). Retrieved from https://agupubs.onlinelibrary.wiley.com/doi/abs/10.1029/2020JC016915 doi: https://doi.org/10.1029/2020JC016915

Kudryavtsev, V., Yurovskaya, M., & Chapron, B. (2021b). Self-similarity of surface wave developments under tropical cyclones. *Journal of Geophysical Research: Oceans*, *126*(4). Retrieved from https://agupubs.onlinelibrary.wiley.com/doi/abs/10.1029/2020JC016916 doi: https://doi.org/10.1029/2020JC016916

Le Merle, E., Hauser, D., Peureux, C., Aouf, L., Schippers, P., Dufour, C., & Dalphinet, A. (2021). Directional and frequency spread of surface ocean waves from swim measurements. *Journal of Geophysical Research: Oceans*, *126*(7). Retrieved from https://agupubs.onlinelibrary.wiley.com/doi/abs/10.1029/2021JC017220 doi: https://doi.org/10.1029/2021JC017220

Li, X., Xu, Y., Liu, B., Lin, W., He, Y., & Liu, J. (2021). Validation and calibration of nadir swh products from cfosat and hy-2b with satellites and in situ observations. *Journal of Geophysical Research: Oceans*, *126*(2), e2020JC016689. Retrieved from https://agupubs.onlinelibrary.wiley.com/doi/abs/10.1029/2020JC016689 (e2020JC016689 2020JC016689) doi: https://doi.org/10.1029/2020JC016689

Lin, I.-I., Rogers, R. F., Huang, H.-C., Liao, Y.-C., Herndon, D., Yu, J.-Y., ... Lien, C.-C. (2021). A tale of two rapidly intensifying supertyphoons: Hagibis (2019) and haiyan (2013). *Bulletin of the American Meteorological Society*, *102*(9), E1645 - E1664. Retrieved from https://journals.ametsoc.org/view/journals/bams/102/9/BAMS-D-20-0223.1.xml doi: 10.1175/BAMS-D-20-0223.1

Moon, I.-J., Ginis, I., Hara, T., Tolman, H. L., Wright, C. W., & Walsh, E. J. (2003). Numerical simulation of sea surface directional wave spectra under hurricane wind forcing. *Journal of Physical Oceanography*, *33*(8), 1680 - 1706. Retrieved from https://journals.ametsoc.org/view/journals/phoc/33/8/2410.1.xml doi: 10.1175/2410.1

Oruba, L., Hauser, D., Planes, S., & Dormy, E. (2022). Ocean waves in the south pacific: Complementarity of swim and sar observations. *Earth and Space Science*, *9*(6), e2021EA002187. Retrieved from https://agupubs.onlinelibrary.wiley.com/doi/abs/10.1029/2021EA002187 doi: https://doi.org/10.1029/2021EA002187

Prakash, K. R., Pant, V., & Nigam, T. (2019). Effects of the sea surface roughness and sea spray-induced flux parameterization on the simulations of a tropical

cyclone. *Journal of Geophysical Research: Atmospheres*, *124*(24), 14037-14058. Retrieved from https://agupubs.onlinelibrary.wiley.com/doi/abs/10.1029/2018JD029760 doi: https://doi.org/10.1029/2018JD029760

Shi, Y., Du, Y., Chu, X., Tang, S., Shi, P., & Jiang, X. (2021). Asymmetric wave distributions of tropical cyclones based on cfosat observations. *Journal of Geophysical Research: Oceans*, *126*(4). Retrieved from https://agupubs.onlinelibrary.wiley.com/doi/abs/10.1029/2020JC016829 doi: https://doi.org/10.1029/2020JC016829

Tamizi, A., Alves, J.-H., & Young, I. R. (2021). The physics of ocean wave evolution within tropical cyclones. *Journal of Physical Oceanography*, *51*(7), 2373 - 2388. Retrieved from https://journals.ametsoc.org/view/journals/phoc/51/7/JPO-D-21-0005.1.xml doi: 10.1175/JPO-D-21-0005.1

Tamizi, A., & Young, I. R. (2020). The spatial distribution of ocean waves in tropical cyclones. *Journal of Physical Oceanography*, *50*(8), 2123 - 2139. Retrieved from https://journals.ametsoc.org/view/journals/phoc/50/8/jpoD200020.xml doi: 10.1175/JPO-D-20-0020.1

Tourain, C., Piras, F., Ollivier, A., Hauser, D., Poisson, J. C., Boy, F., ... Tison, C. (2021). Benefits of the adaptive algorithm for retracking altimeter nadir echoes: Results from simulations and cfosat/swim observations. *IEEE Transactions on Geoscience and Remote Sensing*, *59*(12), 9927-9940. doi: 10.1109/TGRS.2021.3064236

Wright, C. W., Walsh, E. J., Vandemark, D., Krabill, W. B., Garcia, A. W., Houston, S. H., ... Marks, F. D. (2001). Hurricane directional wave spectrum spatial variation in the open ocean. *Journal of Physical Oceanography*, *31*(8), 2472 - 2488. Retrieved from https://journals.ametsoc.org/view/journals/phoc/31/8/1520-0485_2001_031_2472_hdwssv_2.0.co_2.xml doi: 10.1175/1520-0485(2001)031⟨2472:HDWSSV⟩2.0.CO;2

Xu, Y., Hauser, D., Liu, J., Si, J., Yan, C., Chen, S., ... Chen, P. (2022). Statistical comparison of ocean wave directional spectra derived from swim/cfosat satellite observations and from buoy observations. *IEEE Transactions on Geoscience and Remote Sensing*, *60*, 1-20. doi: 10.1109/TGRS.2022.3199393

Ye, J., Wan, Y., & Dai, Y. (2021). Quality evaluation and calibration of the swim significant wave height product with buoy data. *Acta Oceanol. Sol.*, *40*, 187–196. doi: 10.1007/s13131-021-1835-x

Young, I. R. (1998). Observations of the spectra of hurricane generated waves. *Ocean Engineering*, *25*(4), 261-276. Retrieved from https://www.sciencedirect.com/science/article/pii/S0029801897000115 doi: https://doi.org/10.1016/S0029-8018(97)00011-5

Young, I. R. (2006). Directional spectra of hurricane wind waves. *Journal of Geophysical Research: Oceans*, *111*(C8). Retrieved from https://agupubs.onlinelibrary.wiley.com/doi/abs/10.1029/2006JC003540 doi: 10.1029/2006JC003540

Young, I. R. (2017). A review of parametric descriptions of tropical cyclone wind-wave generation. *Atmosphere*, *8*(10). Retrieved from https://www.mdpi.com/2073-4433/8/10/194 doi: 10.3390/atmos8100194

Yurovskaya, M., Kudryavtsev, V., Mironov, A., Mouche, A., Collard, F., & Chapron, B. (2022). Surface wave developments under tropical cyclone goni (2020): Multi-satellite observations and parametric model comparisons. *Remote Sensing*, *14*(9). Retrieved from https://www.mdpi.com/2072-4292/14/9/2032

Zhang, H., He, H., Zhang, W.-Z., & Tian, D. (2021). Upper ocean response to tropical cyclones: a review. *Geoscience Letters*, *8*(1). doi: 10.1186/s40562-020-00170-8

964 # Tables

Table 1. Number of ocean wave spectra measured by SWIM for each TC class in the Northern Hemisphere between May 2019 and August 2021. The number in brackets corresponds to the number of different TC observed. R_{max} is the radius of maximum sustained wind and d is the haversine distance of the observation.

	Slow	Moderate speed	Fast
$0 \leq d/R_{max} < 3$	63 (10)	86 (20)	134 (10)
$3 \leq d/R_{max} < 6$	118 (14)	181 (26)	353 (15)
$6 \leq d/R_{max} < 9$	103 (13)	185 (26)	290 (15)

965 # Figures

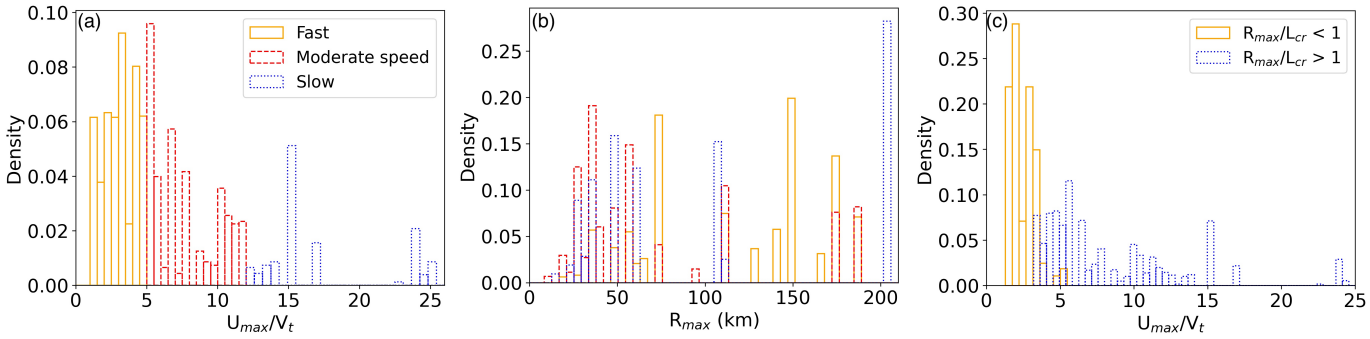

Figure 1. *(a)*: normalized histogram of SWIM observations according to the relative speed U_{max}/V_t. *(b)*: superposition of the normalized histograms of SWIM observations according to the radius of maximum sustained wind speed (R_{max}) for each of the TC class. The colors represent the TC classes as reported in the legend in *(a)*. *(c)*: superposition of the normalized histograms of SWIM observations with the ratio $R_{max}/L_{cr} > 1$ in blue and with the ratio $R_{max}/L_{cr} < 1$ in orange according to the ratio between U_{max}/V_t.

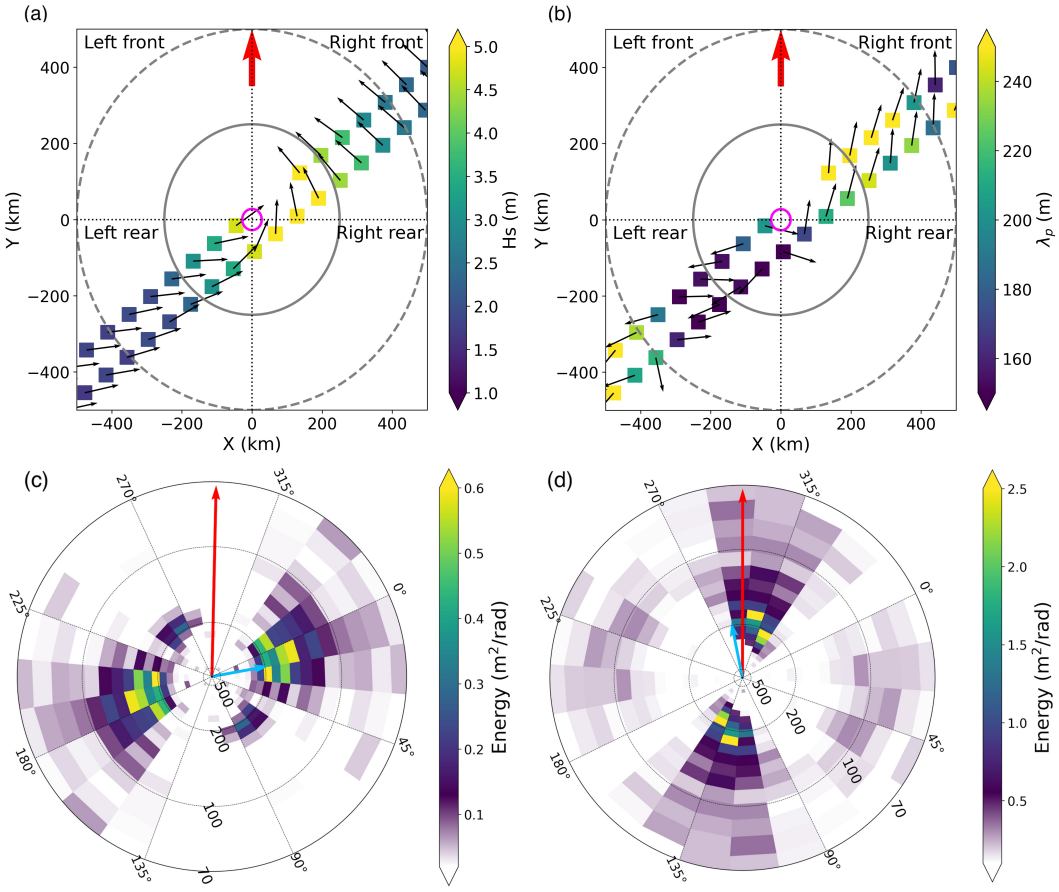

Figure 2. SWIM significant wave height and wind direction *(a)* and dominant wavelength and wave direction *(b)* along the SWIM track over the hurricane Douglas. The track is presented in the tropical cyclone reference frame with the red arrow showing the direction displacement of the hurricane Douglas. The magenta circle stands for the radius of maximum sustained wind speed, the dashed grey circle represents 9 time the radius of maximum sustained wind speed and the solid line grey circle represents a radius of 500 km around the storm position during the SWIM flyover. Bottom panels show wave slope directional spectra obtained on the left side *(c)* and on the right side *(d)* of the TC. The blue arrow shows the wind dominant direction and the red arrow shows the propagation direction of Douglas. 0° stands for North direction.

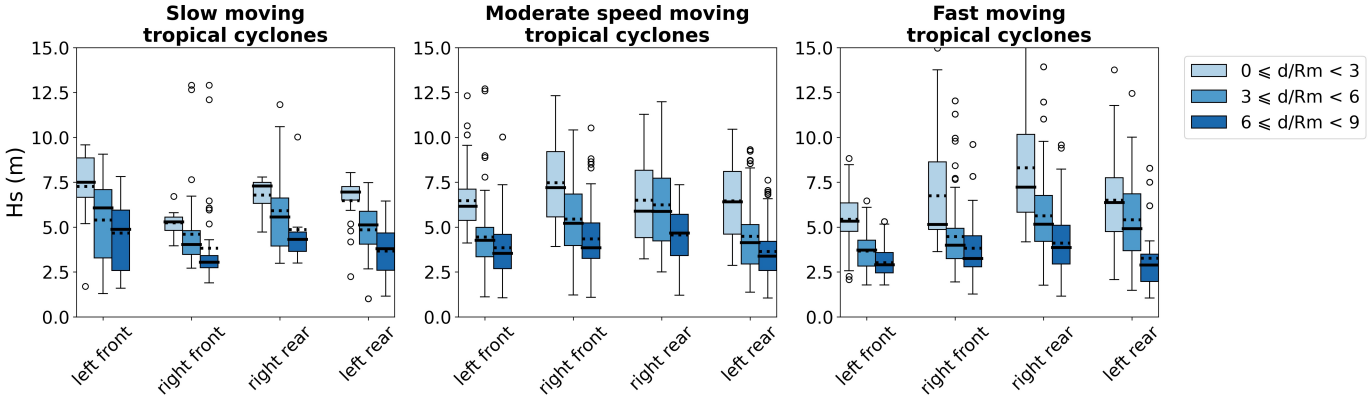

Figure 3. Boxplots showing the distribution of the significant wave height (Hs) for slow (*left panel*), moderate speed (*middle panel*) and fast (*right panel*) moving tropical cyclones in every quadrants as reported on the horizontal axis. The color of the box represents the distance ranges. The boxes represent the distribution of the first to third interquartile range, the error bar stand for and the black circles are the outliers. The solid lines and the dotted lines represent the median and the mean of the distribution, respectively.

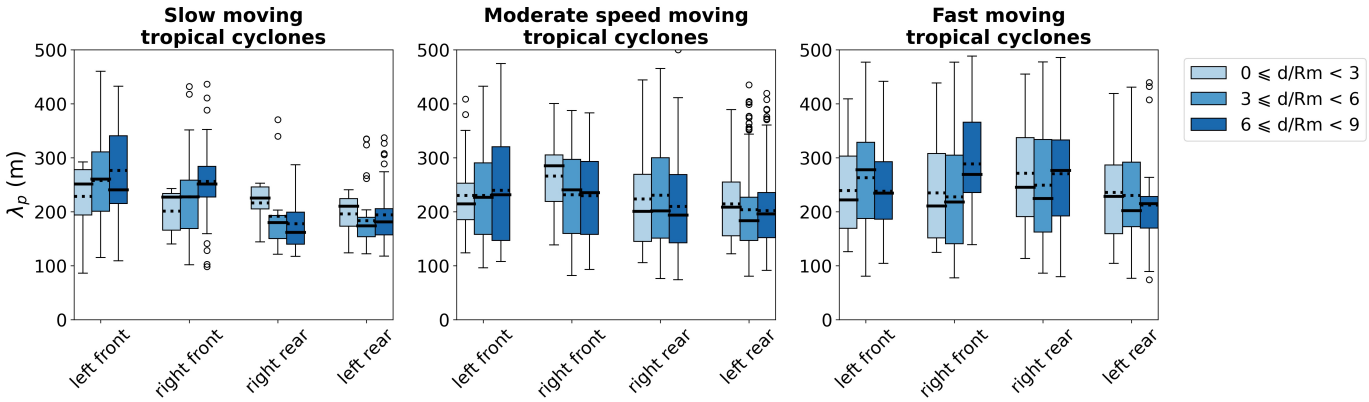

Figure 4. Boxplots showing the distribution of the dominant wavelength (λ_p) of the whole spectrum for slow (*left panel*), moderate speed (*middle panel*) and fast (*right panel*) moving tropical cyclones in every quadrants as reported on the horizontal axis. The figure characteristics are the same as in figure 3.

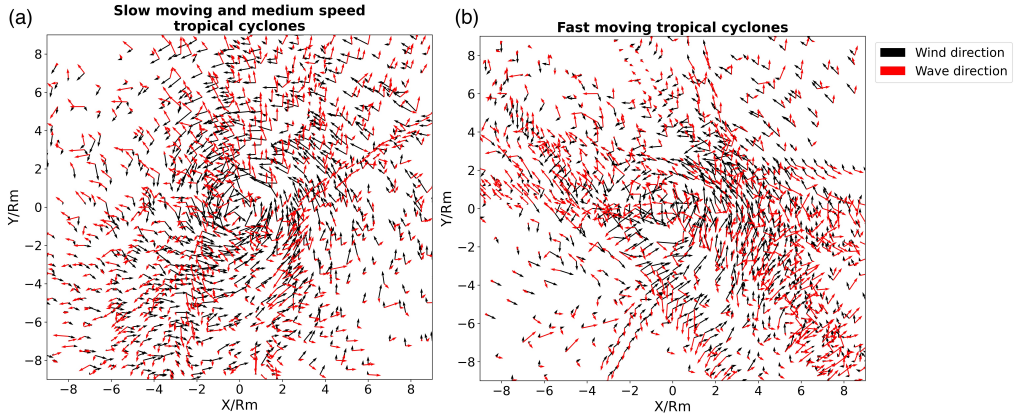

Figure 5. Maps of wind (black) and dominant wave (red) directions in slow-moving and moderate speed *(a)* and in fast-moving *(b)* TC conditions. The length of the arrow corresponds to the wind speed at 10 m according to the ECMWF model and to the dominant wavelength, respectively.

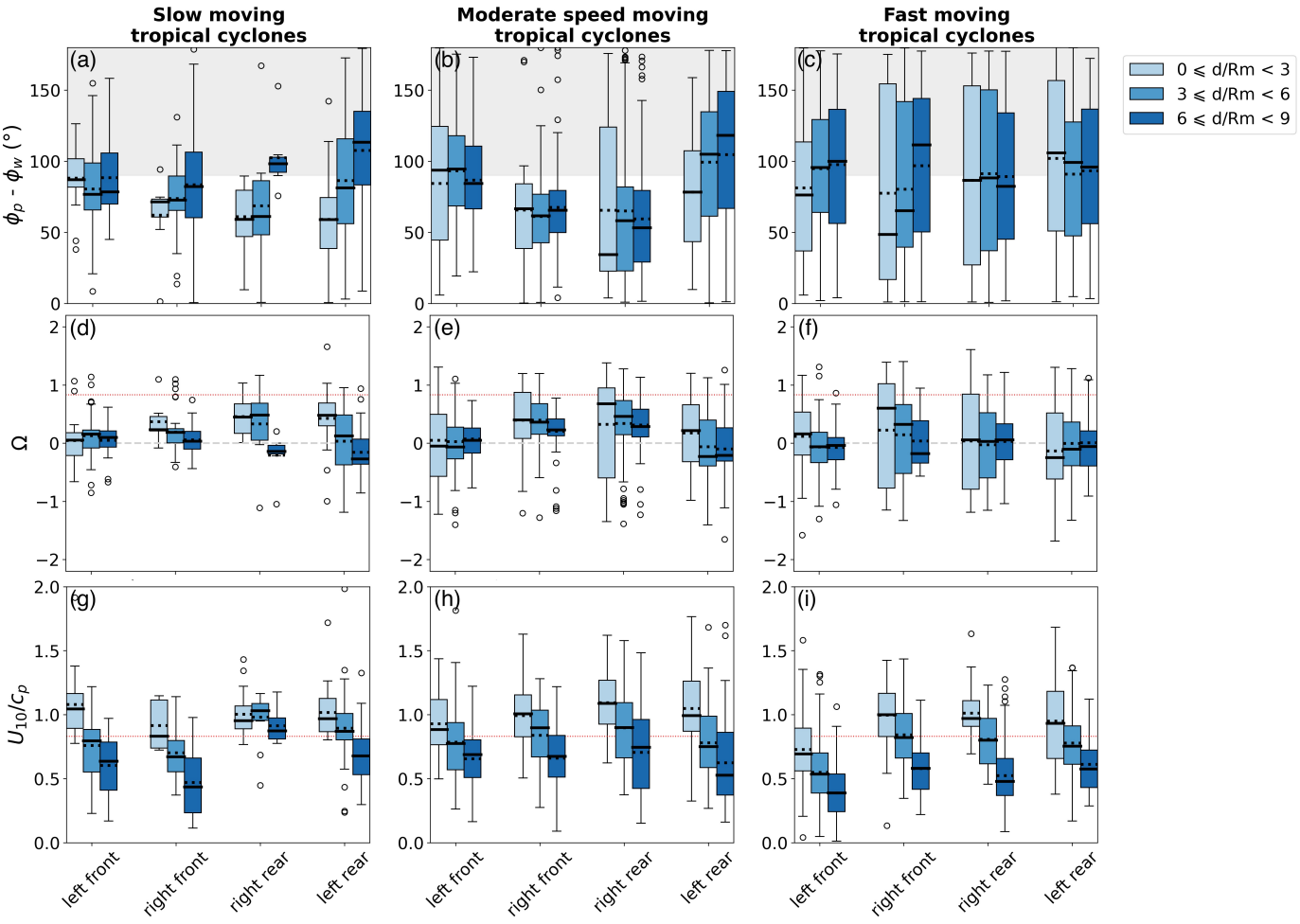

Figure 6. Boxplots showing the distribution of the differences between the dominant wave direction and the wind direction (*top row*), the inverse wave age (Ω) (*middle row*) and U_{10}/C_p (*bottom row*) for slow (*left column*) moderate speed (*middle column*) and fast (*right column*) moving tropical cyclones in every quadrants as reported on the horizontal axis. The figure characteristics are the same as in figure 3. The grey area represents the values higher than 90°, the dashed grey line indicates $\Omega = 0$ and the dotted red line represents the limit between fully and non-fully developed sea (Ω or $U_{10}/C_p = 0.83$).

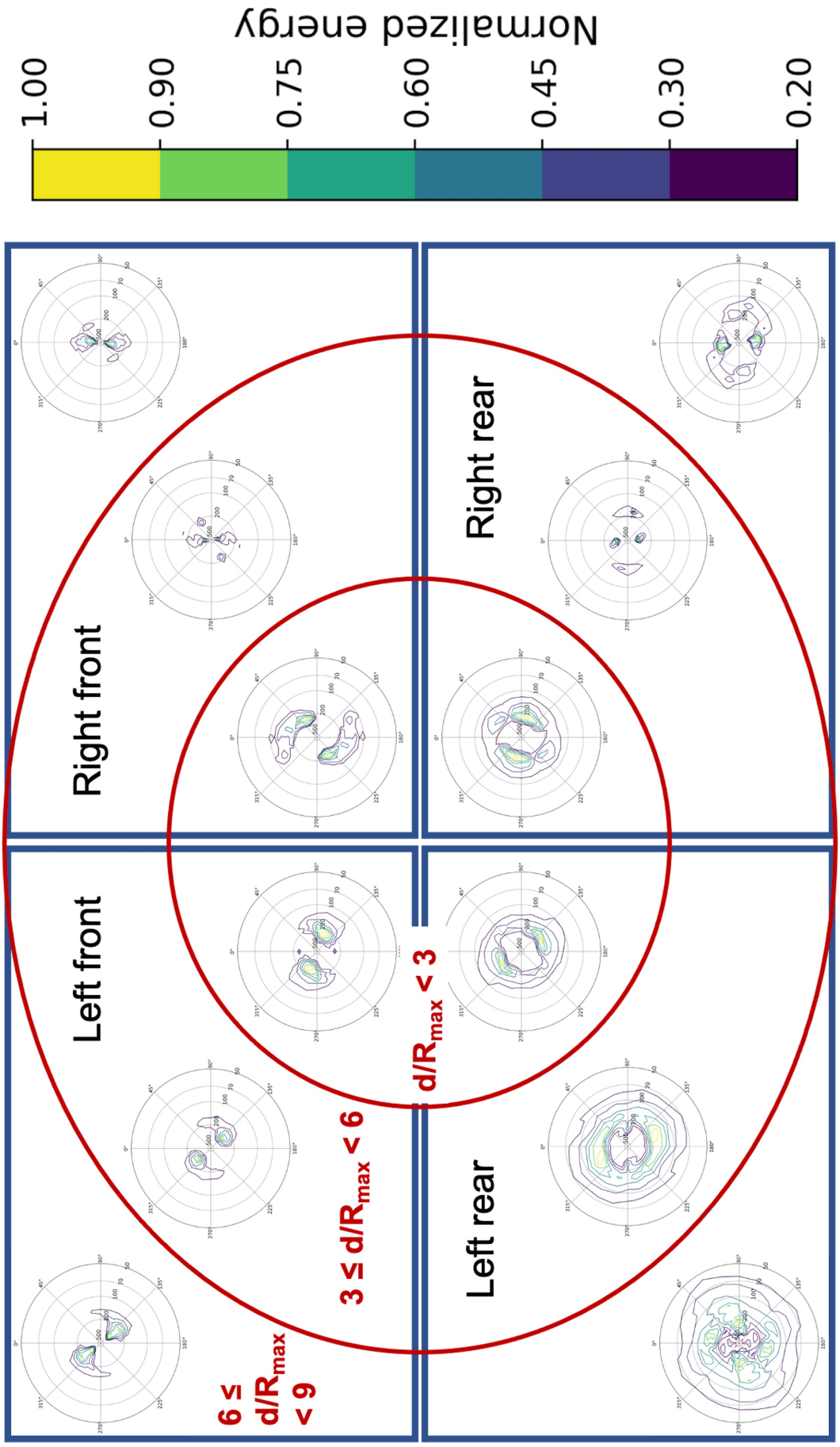

Figure 7. Average normalized wave height directional spectra in case of slow-moving tropical cyclones. Each blue square represents a quadrant and the red circles stand for the distance

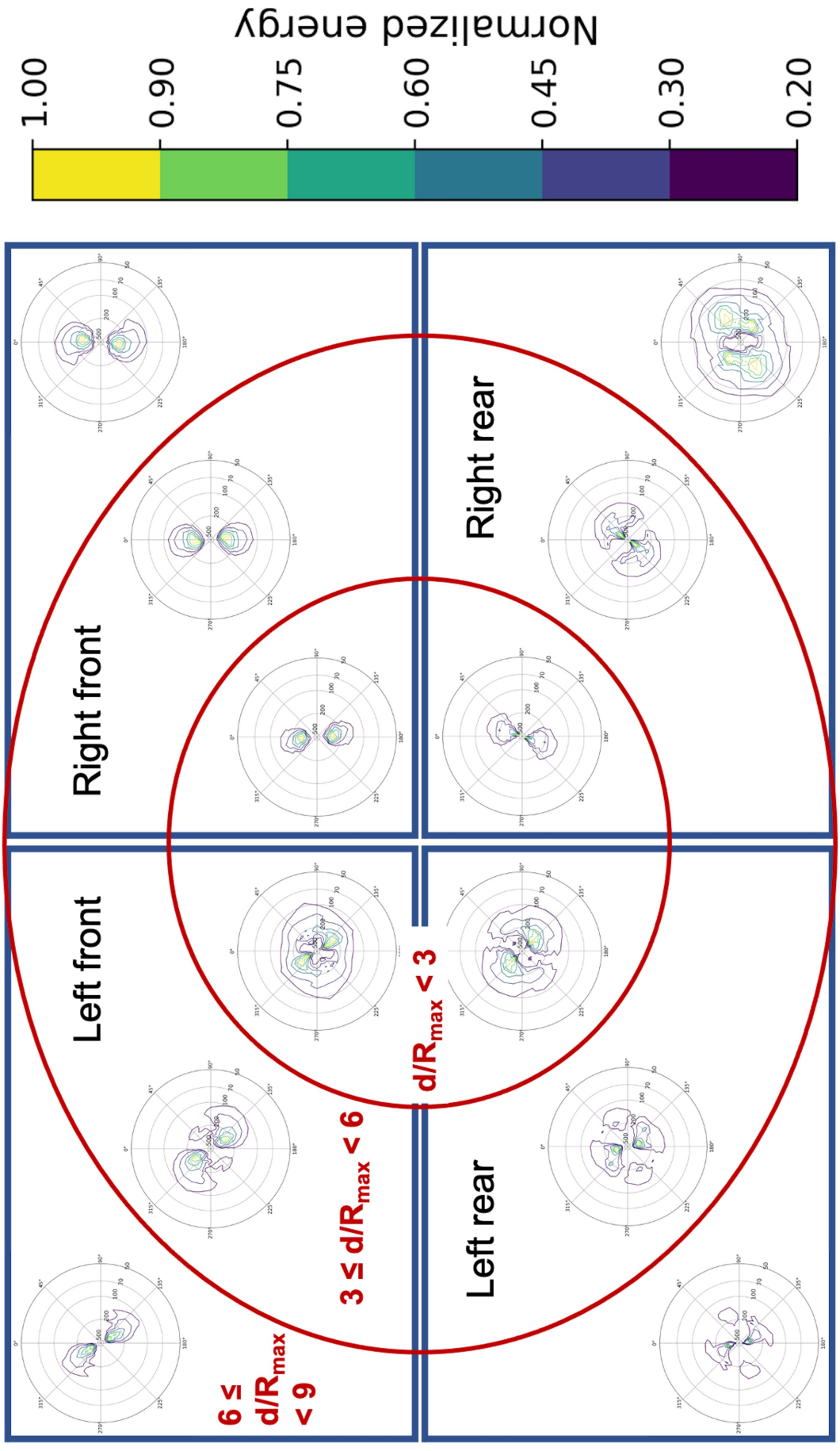

Figure 8. Average normalized wave height directional spectra in case of moderate speed tropical cyclones. Each blue square represents a quadrant and the red circles stand for the distance

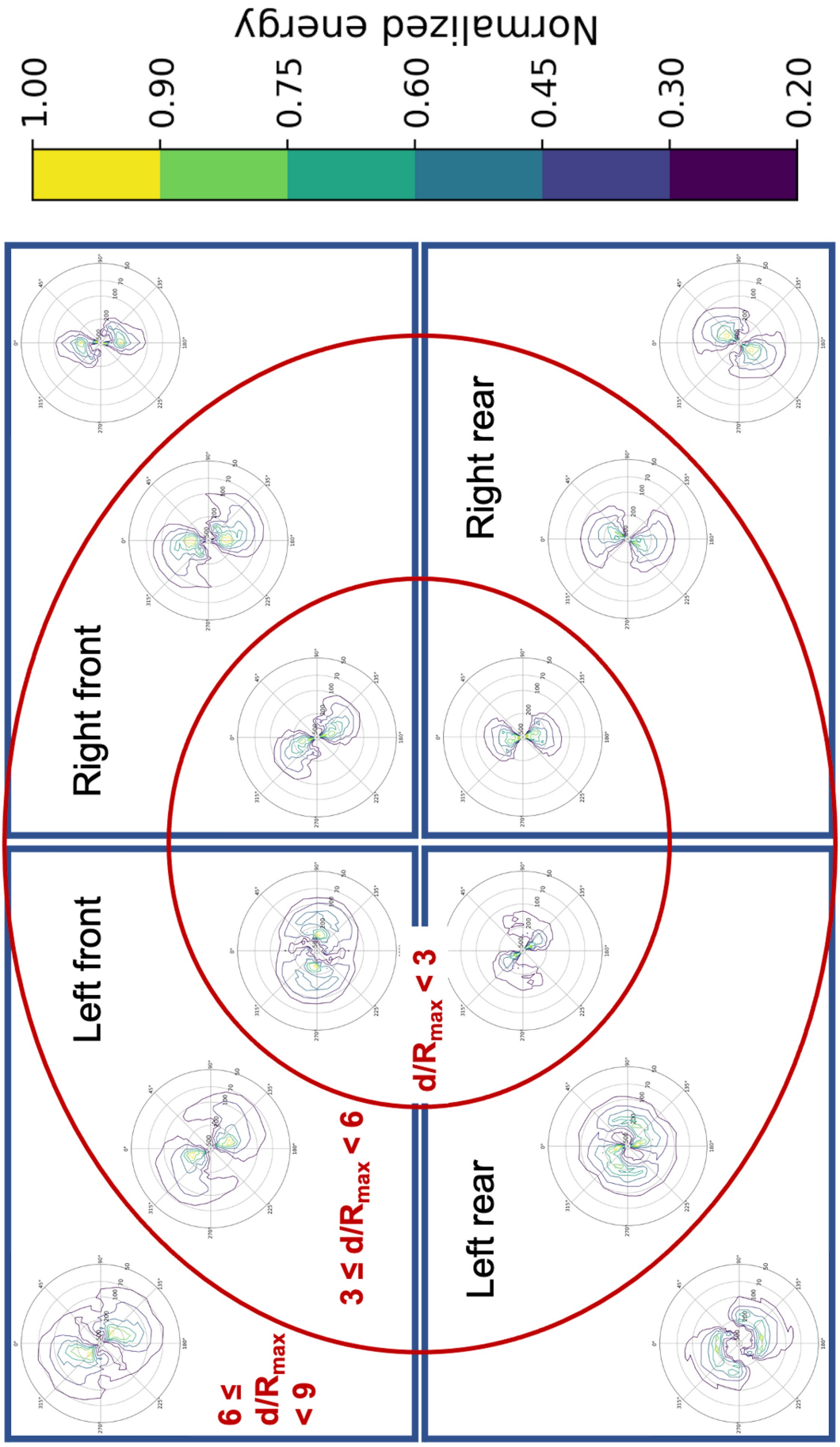

Figure 9. Average normalized wave height directional spectra in case of fast-moving tropical cyclones. Each blue square represents a quadrant and the red circles stand for the distance

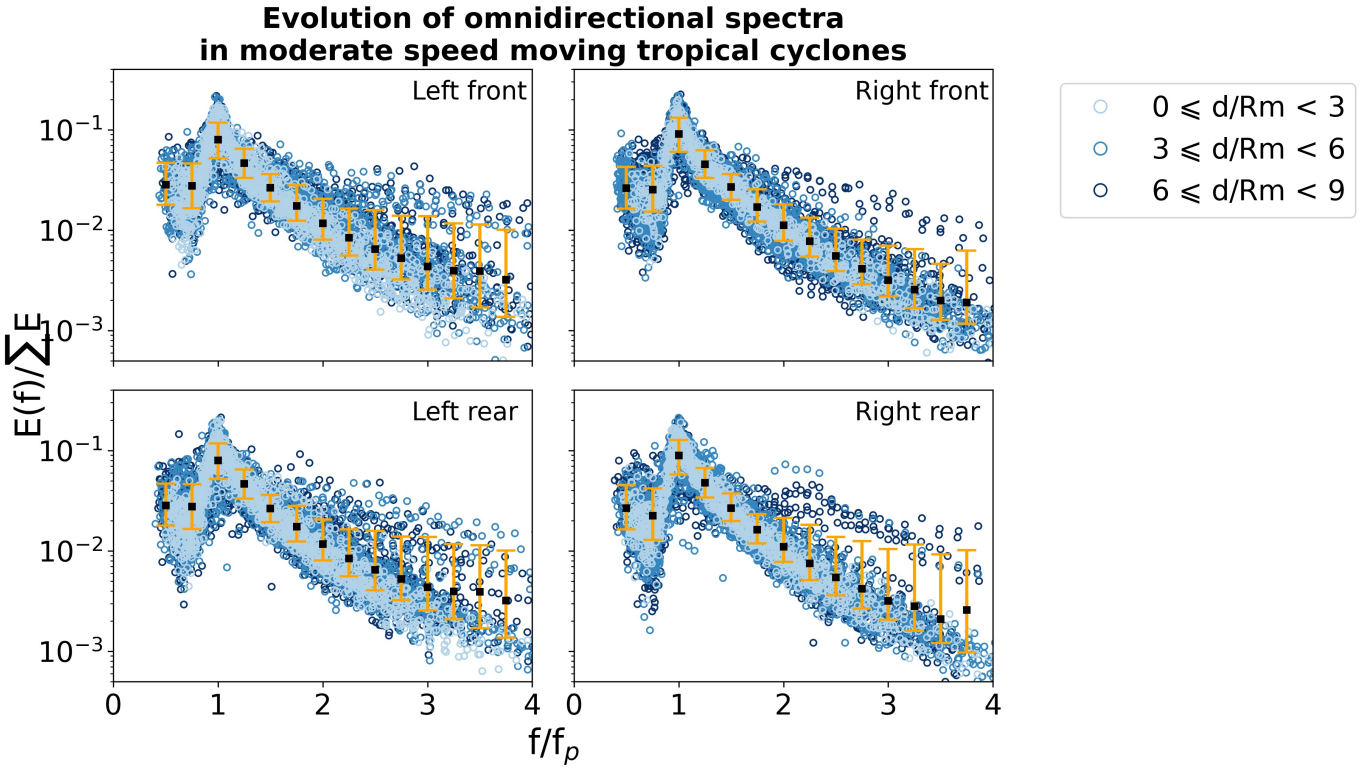

Figure 10. Omni-directional wave height spectra as a function of the normalized frequency (f/f_p) for each quadrant under moderate speed tropical cyclone conditions. The energy of the spectra is normalized with the total energy. The color of the circles correspond to the distance ranges as reported in the legend. The black squares and the orange error bars represent the mean and the standard deviation of the spectra for every bin of 0.25 f/f_p.

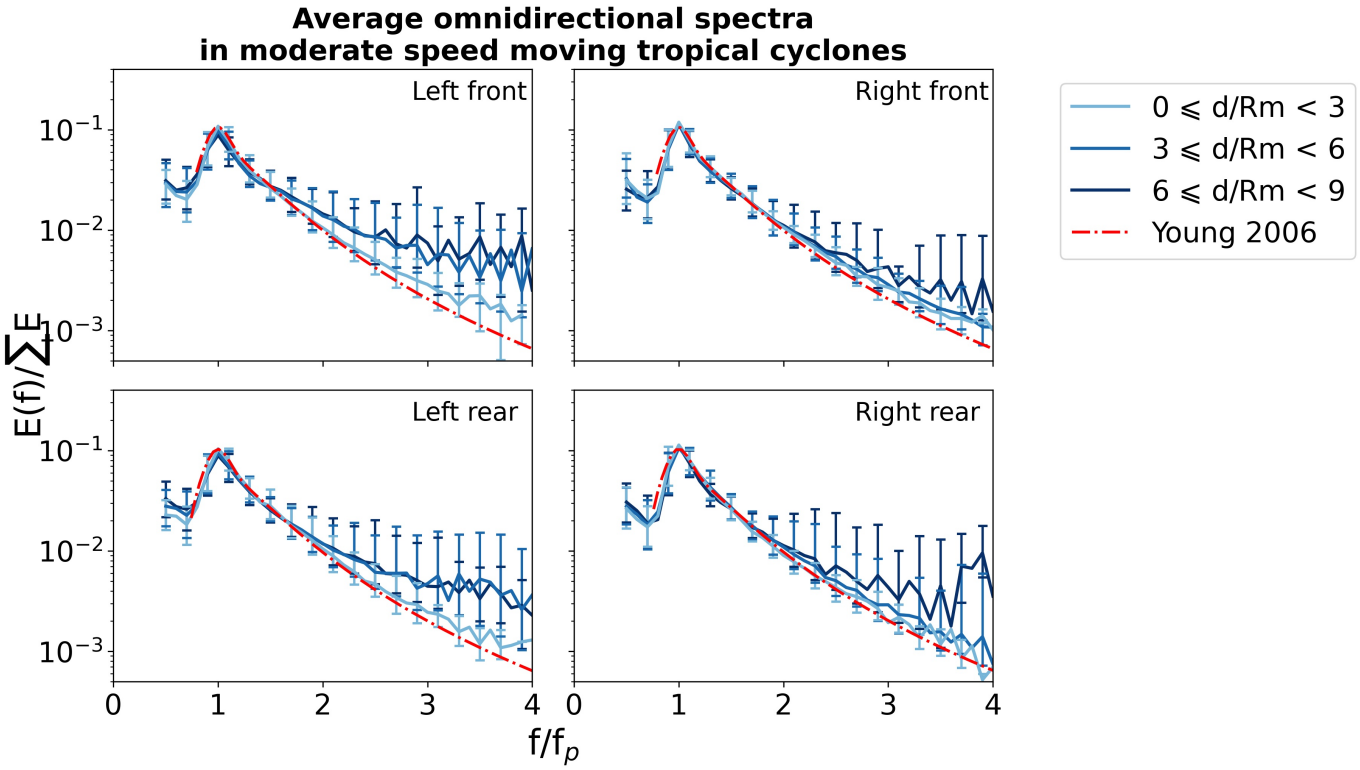

Figure 11. Average omni-directional spectra as a function of the normalized frequency (f/f_p) for each quadrant under moderate speed tropical cyclone conditions. The energy of the spectra is normalized with the total energy. The color of the lines, squares and error bars correspond to the distance ranges as reported in the legend. The red dashed-dotted line corresponds to the JONSWAP spectrum adjusted by Young (2006).

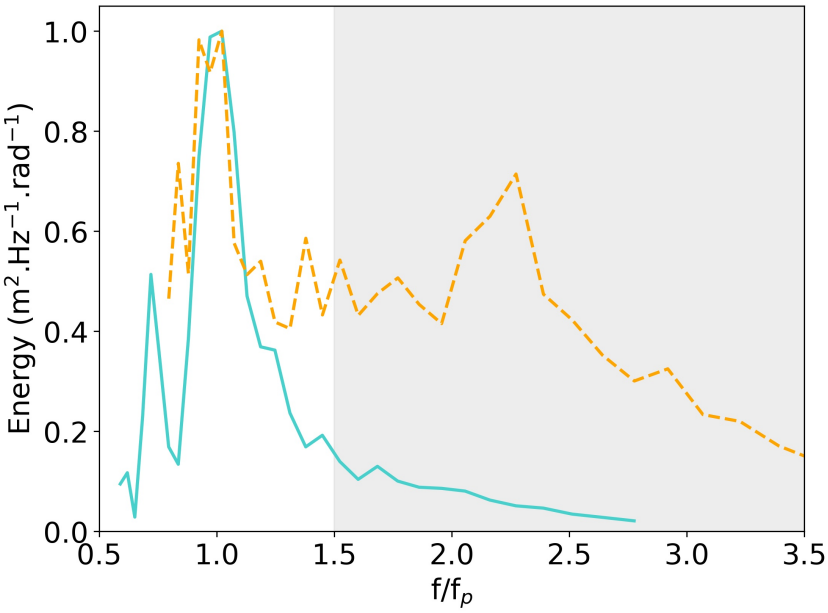

Figure 12. Examples of SWIM omni-directional frequency wave height spectrum as a function of f/f_p obtained in moderate speed moving TC at distances larger than 6 R_{max}.The grey area indicates the portion of the spectrum over which is calculated the n factor. The spectra are normalized according to their respective maximum of energy.

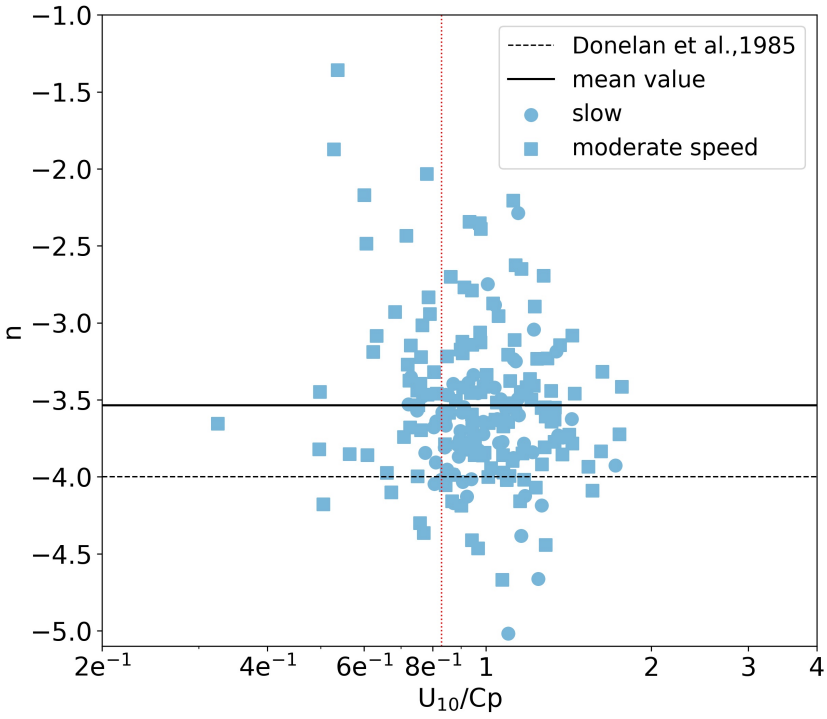

Figure 13. Variation of the frequency decay exponent n with U_{10}/C_p for observations at less than 3 R_{max} in slow (circle symbol) and moderate speed (square symbol) moving TCs. The black line shows the mean values of the SWIM data, the black dashed line shows the mean value obtained by Donelan et al. (1985), in fetch-limited conditions (n = -4) and the red dotted line indicates the limit value of U_{10}/C_p = 0.83 separating young wind sea and swell.

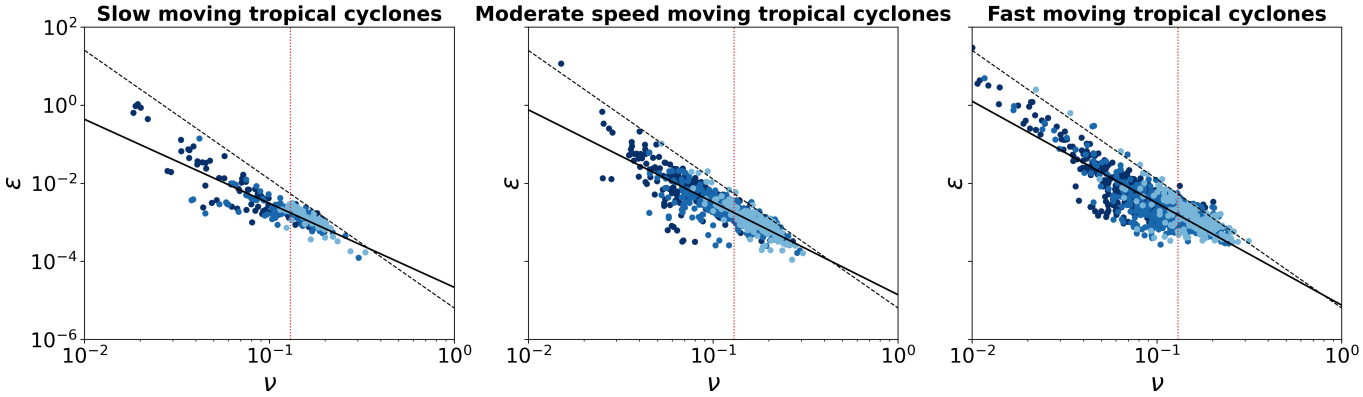

Figure 14. Variation of the non-dimensional frequency ν with the non-dimensional energy ϵ for *(a)* slow, *(b)* moderate and *(c)* fast-moving TCs. The color of the symbol corresponds to the distance ranges following the same convention as in the previous figures. The black dashed line shows the relationship estimated by Donelan et al. (1985) and the red dashed line indicates the limit value of $\nu = 0.13$ separating young wind sea and swell.